

HD molecules at high redshift: cosmic-ray ionization rate in the diffuse interstellar medium

D. N. Kosenko,^{1*} S. A. Balashev,^{1†} P. Noterdaeme², J.-K. Krogager²,
R. Srianand³ and C. Ledoux⁴

¹*Ioffe Institute, 26 Politeknicheskaya st., St. Petersburg, 194021, Russia*

²*Institut d'Astrophysique de Paris, UMR 7095, CNRS-SU, 98bis boulevard Arago, 75014 Paris, France*

³*Inter-University Centre for Astronomy and Astrophysics, Post Bag 4, Ganeshkhind, 411 007, Pune, India*

⁴*European Southern Observatory, Alonso de Córdova 3107, Vitacura, Casilla 19001, Santiago, Chile*

Accepted XXX. Received YYY; in original form ZZZ

ABSTRACT

We present a systematic study of deuterated molecular hydrogen (HD) at high redshift, detected in absorption in the spectra of quasars. We present four new identifications of HD lines associated with known H₂-bearing Damped Lyman- α systems. In addition, we measure upper limits on the HD column density in twelve recently identified H₂-bearing DLAs. We find that the new HD detections have similar $N(\text{HD})/N(\text{H}_2)$ ratios as previously found, further strengthening a marked difference with measurements through the Galaxy. This is likely due to differences in physical conditions and metallicity between the local and the high-redshift interstellar media. Using the measured $N(\text{HD})/N(\text{H}_2)$ ratios together with priors on the UV flux (χ) and number densities (n), obtained from analysis of H₂ and associated C I lines, we are able to constrain the cosmic-ray ionization rate (CRIR, ζ) for the new HD detections and for eight known HD-bearing systems where priors on n and χ are available. We find significant dispersion in ζ , from a few $\times 10^{-18} \text{ s}^{-1}$ to a few $\times 10^{-15} \text{ s}^{-1}$. We also find that ζ strongly correlates with χ – showing almost quadratic dependence, slightly correlates with Z , and does not correlate with n , which probably reflects a physical connection between cosmic rays and star-forming regions.

Key words: Quasars: absorption lines; galaxies: ISM; ISM: molecules; cosmic rays

1 INTRODUCTION

The formation and evolution of galaxies is intimately linked to their interstellar medium (ISM). Indeed, the ISM provides the fuel for star formation and in turn, the physical and chemical properties of the ISM are affected by stars (through UV radiation, cosmic rays, winds, enrichment by metals and dust, mechanical energy injection, etc.). The ISM presents several phases: the cold dense phases (cold neutral medium, CNM, itself including molecular phases) that may eventually collapse to form stars, the warmer, less dense phases (warm neutral and ionized medium, WNM and WIM, respectively), and the hot ionized medium (HIM) (Field et al. 1969; McKee & Ostriker 1977). These phases are well studied in the local Universe via analysis of emission over a large range of wavelengths in the electromagnetic spectrum from X-ray (Snowden et al. 1997) to radio (Heiles & Troland 2003), but their description is still limited at high redshift, due to flux

dimming at cosmological distances and significantly coarser spatial resolution available for emission-line studies of most tracers of the ISM.

This problem can be overcome by absorption-line spectroscopy. Both the WNM and CNM at high redshift are detectable in the spectra of background quasars and γ -ray burst (GRB) afterglows as Damped Lyman- α systems (DLAs) – absorption-line systems with the highest column densities of neutral hydrogen, H I ($\log N(\text{H I}) > 20.3^1$) and a collection of associated metal lines (for a review, see Wolfe et al. 2005). Most DLAs actually represent WNM (Srianand et al. 2005; Neeleman et al. 2015), while CNM is much more rarely detected (in a few percent of DLAs, see e.g., Balashev & Noterdaeme 2018).

One of the main tracers of CNM is molecular hydrogen (H₂), the most abundant molecule in the Universe. Using UV absorption lines of H₂ in the Lyman and Werner bands, one can probe diffuse and translucent molecular clouds along

* E-mail: kosenkodn@yandex.ru

† E-mail: s.balashev@gmail.com

¹ Here and in what follows, N is the column density in cm^{-2} .

the line of sight (Ledoux et al. 2003; Noterdaeme et al. 2008, 2010; Balashev et al. 2017; Ranjan et al. 2018). If the H_2 column density is large enough, the less abundant isotopologue, HD, can also be detected (Varshalovich et al. 2001). To date, HD lines have been detected only in twelve intervening systems among ~ 40 confirmed H_2 -bearing DLAs at high redshift ($z > 0$) (Noterdaeme et al. 2008; Balashev et al. 2010; Tumlinson et al. 2010; Ivanchik et al. 2010; Noterdaeme et al. 2010; Klimenko et al. 2015; Ivanchik et al. 2015; Klimenko et al. 2016; Noterdaeme et al. 2017; Balashev et al. 2017; Rawlins et al. 2018; Kosenko & Balashev 2018). This number remains limited since the detailed analysis of H_2 and HD lines can be done only in high-resolution quasar spectra, which require observations with the largest optical telescopes. Also, as mentioned before, the incident rate of the cold ISM in DLAs at high z is quite low. Hence, blind searches for HD/ H_2 are very inefficient (Jorgenson et al. 2014). Notwithstanding, in recent years several efficient techniques were proposed to pre-select saturated H_2 lines in DLAs where HD is then easier to detect (Balashev et al. 2014; Ledoux et al. 2015; Noterdaeme et al. 2018).

Some of the high-redshift $N(\text{HD})/2N(\text{H}_2)$ measurements lie close to the primordial isotopic $(\text{D}/\text{H})_p$ ratio, triggering discussion on whether the molecular isotopic ratio could serve as a proxy for D/H, in particular at high column densities where the cloud is thought to be fully molecularized (e.g., Ivanchik et al. 2010). However, models suggest that the HD/ H_2 ratio varies significantly with depth into the clouds (Le Petit et al. 2002; Liszt 2015; Balashev & Kosenko 2020) since HD and H_2 have different main formation mechanisms: H_2 is forming mainly on the surface of dust grains, while HD is mostly formed via fast ion-molecular reactions. At the same time, destruction of both HD and H_2 mainly occurs via photo-dissociation by UV photons.² This implies that the HD/ H_2 ratio is sensitive to a combination of physical conditions, and that the HD/ H_2 ratio can differ from the isotopic ratio even at high column densities in self-shielded regions (Balashev & Kosenko 2020). Moreover, under some conditions the D/HD transition may take place earlier than the H/ H_2 transition (Balashev & Kosenko 2020), which leads to $\text{HD}/2\text{H}_2 > \text{D}/\text{H}$ (Tumlinson et al. 2010; Noterdaeme et al. 2017), and therefore HD/ H_2 may not be used as a lower limit for the isotopic ratio.

From the known HD-bearing systems, it was found that the relative HD/ H_2 abundance tends to systematically be higher at high redshift than in the Galaxy (Snow et al. 2008; Balashev et al. 2010; Tumlinson et al. 2010; Ivanchik et al. 2015). This discrepancy cannot be solely explained by the progressive destruction of deuterium, since the astration of D through stellar evolution is expected to be small (Dvorkin et al. 2016). Therefore, the most probable explanation is to be sought in differences in physical conditions between the ISM of the Galaxy and that of distant galaxies. Indeed, models of ISM chemistry show that the HD/ H_2 ratio is sensitive to the physical conditions in the ISM – UV flux, cosmic-ray ionization rate (CRIR), metallicity, number density, and

cloud depth (Le Petit et al. 2002; Ćirković et al. 2006; Liszt 2015; Balashev & Kosenko 2020). Among these parameters, the cosmic-ray ionization rate seems to play a major role, being extremely important for the ISM chemistry. Indeed, cosmic rays are an important source of heating and the main ionizing source and therefore drives almost all the chemistry in the ISM. In the case of HD, cosmic rays promote the main channel of its formation as follows:



Therefore, HD can, in principle, be used to constrain the CRIR (e.g., Balashev & Kosenko 2020). Such independent constraint would be extremely valuable, given the still loose constraints on CRIR in both the local Universe (see, e.g., Hartquist et al. 1978; van Dishoeck & Black 1986; Federman et al. 1996; Indriolo et al. 2007; Neufeld & Wolfire 2017; González-Alfonso et al. 2013, 2018; van der Tak et al. 2016) and at high redshift (Muller et al. 2016; Shaw et al. 2016; Indriolo et al. 2018). Additionally, a HD-based method to constrain CRIR has an important advantage compared to other, widely-used methods based on oxygen-bearing molecules: the abundance of HD is found to increase relative to H_2 when the metallicity decreases (mostly due to chemistry; Liszt 2015; Balashev & Kosenko 2020). Therefore, HD allows us to probe the CNM in lower metallicity environments.

Motivated by this emerging new possibility of using HD as a probe of CRIR and the lack of known HD detections to date, we performed a systematic search for HD in recently-published and archival H_2 -bearing DLAs at high redshift. We report four new HD detections. Additionally, we refit HD, H_2 , and C I in a few systems to obtain confidence upper limits on HD column density and to get consistent constraints on its physical parameters. Finally, in one DLA we find H_2 that has not been reported before (while we only obtain an upper limit on HD). This paper is organized as follows: in Sect. 2 we present the sample in which we searched for HD lines. Sect. 3 describes the data analysis and details on individual systems. The measurements of HD/ H_2 abundances are summarized in Sect. 4 and used in Sect. 5 to constrain the physical conditions in the absorbing medium. In Sect. 6, we discuss some implications on the derived CRIR and limitations of the model. Lastly, in Sect. 7 we offer our concluding remarks.

2 DATA

To search for HD absorption lines in high- z DLAs, we used quasar spectra obtained at medium and high resolving power with X-shooter ($R \sim 6000$; Vernet et al. 2011) and the Ultraviolet and Visual Echelle Spectrograph (UVES, $R \sim 50\,000$; Dekker et al. 2000) on the Very Large Telescope (VLT) as well as the High Resolution Echelle Spectrograph (HIRES, $R \sim 50\,000$; Vogt et al. 1994) on the Keck telescope.

Most of the data come from X-shooter and include the spectra of quasars with recently reported high- z H_2 -bearing DLAs from Noterdaeme et al. (2018); Ranjan et al. (2018); Balashev et al. (2019); Ranjan et al. (2020). The detailed description of the observations and data reduction is presented in the above-mentioned papers. Typically, these quasars were observed with 1-4 exposures, each about one hour long.

² Photo-dissociation is the main destruction process for molecules but there can be additional reactions such as destruction by cosmic rays or reversed reaction (Eq. 2) that lead to a non-unity molecular fraction even in the fully self-shielded part of the clouds.

The UVES data include the system at $z = 3.09$ towards J1311+2225, recently reported by [Noterdaeme et al. \(2018\)](#), where C I together with H₂ and CO molecules were detected, the well-known three ESDLA systems at $z = 2.402$ towards HE0027–1836 ([Noterdaeme et al. 2007](#)) (for which further data was obtained by [Rahmani et al. \(2013\)](#), leading to an improved quality spectrum), at $z = 3.85$ towards J0816+1446 ([Guimarães et al. 2012](#)), at $z = 2.48$ towards J2140–0321 ([Noterdaeme et al. \(2010\)](#)), and the DLA system towards J2340–0053 where HD was reported independently and almost simultaneously by [Kosenko & Balashev \(2018\)](#) and [Rawlins et al. \(2018\)](#). For this latter system, we refitted HD together with H₂ and C I lines to obtain self-consistent priors on physical parameters that are used to derive the CRIR. For these systems we used the spectra from original publications or the SQUAD UVES database ([Murphy et al. 2019](#)), or from KODIAQ DR2 database ([O’Meara et al. 2017](#)).

We also looked at all other known H₂-bearing DLAs at high z to search for HD absorption lines that were not detected or considered in the original studies. [Kosenko & Balashev \(2018\)](#) reported a new H₂-bearing system at $z = 2.067$ towards Q0812+3208. Unfortunately, only the weakest HD transition (L0-0 band) is covered by the HIRES spectrum (see details by [Balashev et al. 2010](#)), so that we were only able to place an upper limit on $N(\text{HD})$.

A summary of the H₂-bearing DLAs analysed in this paper is provided in Table 1. In Table 2, we provide information on previously known high- z HD/H₂-bearing systems known to date, that were used later to derive physical conditions.

3 ANALYSIS

We analyzed the absorption lines using multi-component Voigt profile³ fitting. The unabsorbed continuum was typically constructed by-eye using spline interpolation constrained by the regions free from any evident absorption lines (see e.g. [Balashev et al. 2019](#)). The lines were fitted simultaneously and the spectral pixels that were used to constrain the model were selected by eye to avoid blends (mainly with Ly- α forest lines). The best value and interval estimates on the fitting parameters (Doppler parameter, b , column density, N and redshift, z) were obtained with a Bayesian approach, using standard χ^2 likelihood to compare the data and the model. To sample the posterior distribution function of the parameters we used Monte Carlo Markov Chain (MCMC) (see e.g. [Balashev et al. 2017](#)) with affine-invariant sampling ([Goodman & Weare 2010](#)). By default the priors on most parameters were assumed to be flat (for b , $\log N$ and z). However, for most X-shooter spectra, the resolution is not high enough to accurately resolve the velocity structure and some HD lines can be in the saturated regime. In these cases, we found that column densities and Doppler parameters can be highly degenerated, resulting in uncertain constraints. Therefore, we used priors on

the number of components, their redshifts and Doppler parameters from the analysis of H₂ or C I absorption lines (see e.g. [Balashev et al. 2019](#)). This is adequate, since H₂ is usually constrained by a large number of lines ($\sim 50 - 100$) and C I is fitted in the region out of Ly α forest. We used mostly components where the column density of H₂ exceeds $\log N(\text{H}_2) \gtrsim 18$, since for lower H₂ columns, the expected HD column densities will be much lower than what the data can constrain, i.e. even upper limits will be uninformative.

Moreover, we found that in X-Shooter spectra, the continuum placement for some HD lines is non-trivial. We estimated the resulting uncertainty independently using the following procedure. We performed a large number (~ 500) of realizations, where we randomly shifted the continuum level for each line. The values of the shifts were drawn from a normal distribution with dispersion corresponding to the mean uncertainty of spectral pixels at the positions of absorption lines. For each realization, we also randomly drew an HD Doppler parameter using constraints obtained from H₂. The redshift uncertainty from H₂ (or C I) in most cases is quite low and has only marginal effect on the results. We then fitted each realization i with fixed b and z and obtained the best fit column density $N^i(\text{HD})$. We obtained the final HD column density measurement from the distribution of $N^i(\text{HD})$. We found that the uncertainties on HD column densities increase in most cases by a factor of ~ 2 compared to MCMC fit with fixed continuum, meaning that the continuum placement uncertainty contributes significantly to the total $N(\text{HD})$ uncertainty budget at medium resolution.

We summarize the results of fitting HD lines in Table 3 and provide specific comments on each system as follows:

3.1 VLT/X-shooter data:

3.1.1 J0136+0440

We only tentatively detected HD absorption lines at the expected positions based on the redshift of the main H₂ component ($z = 2.779430$) with column density $\log N(\text{H}_2) = 18.64^{+0.06}_{-0.08}$ and Doppler parameter $b = 7.7^{+2.4}_{-1.9} \text{ km s}^{-1}$. Therefore, fixing z and using priors on Doppler parameter from H₂ analysis, we placed only an upper limit to the HD column density in this component, $\log N(\text{HD}) < 14.5$. The fits to the unblended HD absorption lines are shown in Fig. A1. Here and in the following figures we show only those HD absorption lines that are not totally blended with other absorption lines (from Ly α forest and/or H₂ and metal lines from corresponding DLA).

3.1.2 J0858+1749

We detected HD absorption lines at the position of H₂ component ($z = 2.62524$) that has $\log N(\text{H}_2) = 19.72^{+0.01}_{-0.02}$ and $b = 7.9^{+0.4}_{-0.4} \text{ km s}^{-1}$. To fit HD lines we fixed z and used b as a prior from H₂ analysis. Using the HD L8-0R(0) line and red wings of HD L4-0R(0), HD L7-0R(0), HD L11-0R(0) and HD L12-0R(0) absorption lines (see Fig. A2), we constrained $\log N(\text{HD}) = 14.87^{+0.06}_{-0.09}$.

³ The Voigt profile is a convolution of Lorentzian and Gaussian functions, arising from natural broadening and thermal/turbulent motions of the gas, respectively.

Table 1. H₂-bearing DLA systems searched for HD.

| Quasar | z_{em} | z_{abs} | $\log N(\text{HI})$ | $[\text{X}/\text{H}]^a$ | X | $\log N(\text{H}_2)$ | References ^b |
|---|-----------------|------------------|---------------------|-------------------------|----|-------------------------|-------------------------|
| VLT/X-shooter data: | | | | | | | |
| J 0136+0440 | 2.78 | 2.779 | 20.73 ± 0.01 | -0.58 ± 0.03 | S | $18.65^{+0.06}_{-0.07}$ | 1 |
| J 0858+1749 | 2.65 | 2.625 | 20.40 ± 0.01 | -0.63 ± 0.02 | S | $19.72^{+0.01}_{-0.02}$ | 1 |
| J 0906+0548 | 2.79 | 2.567 | 20.13 ± 0.01 | $-0.18^{+0.05}_{-0.08}$ | S | 18.88 ± 0.02 | 1 |
| J 0917+0154 | 2.18 | 2.107 | 20.75 ± 0.04 | 0.17 ± 0.07 | Zn | 20.11 ± 0.06 | 2, 3 |
| J 0946+1216 | 2.66 | 2.607 | 21.15 ± 0.02 | -0.48 ± 0.01 | S | $19.97^{+0.01}_{-0.02}$ | 1 |
| J 1143+1420 | 2.58 | 2.323 | 21.64 ± 0.06 | -0.80 ± 0.06 | Zn | 18.3 ± 0.1 | 4 |
| J 1146+0743 | 3.03 | 2.840 | 21.54 ± 0.01 | -0.57 ± 0.02 | Zn | $18.82^{+0.03}_{-0.02}$ | 1 |
| J 1236+0010 | 3.02 | 3.033 | 20.78 ± 0.01 | $-0.58^{+0.04}_{-0.03}$ | S | 19.76 ± 0.01 | 1 |
| J 1513+0352 | 2.68 | 2.46 | 21.83 ± 0.01 | -0.84 ± 0.23 | Zn | 21.31 ± 0.01 | 5 |
| J 2232+1242 | 2.30 | 2.230 | 21.75 ± 0.03 | -1.48 ± 0.05 | Zn | 18.56 ± 0.02 | 4 |
| J 2347-0051 | 2.62 | 2.588 | 20.47 ± 0.01 | $-0.60^{+0.06}_{-0.09}$ | S | 19.44 ± 0.01 | 1 |
| High-resolution (Keck/HIRES and VLT/UVES) data: | | | | | | | |
| HE0027-1836 | 2.56 | 2.402 | 21.75 ± 0.10 | -1.63 ± 0.10 | Zn | 17.43 ± 0.02 | 4, 6 |
| J 0812+3208 | 2.70 | 2.067 | 21.50 ± 0.20 | -1.83 ± 0.20 | Si | 19.28 ± 0.01^c | 7, 8 |
| J 0816+1446 | 3.85 | 3.287 | 22.00 ± 0.10 | -1.10 ± 0.10 | Zn | 18.48 ± 0.02^c | 9 |
| J 1311+2225 | 3.14 | 3.093 | 20.62 ± 0.10 | $-0.34^{+0.13}_{-0.14}$ | Zn | 19.69 ± 0.01^c | 2 |
| J 2140-0321 | 2.48 | 2.339 | 22.41 ± 0.03 | -1.52 ± 0.08 | Zn | 20.13 ± 0.07 | 4, 10 |

(a) Metallicity with respect to solar (Asplund et al. 2009): $[\text{X}/\text{H}] = \log(\text{X}/\text{H}) - \log(\text{X}/\text{H})_{\odot}$.

(b) References: (1) Balashev et al. (2019), (2) Noterdaeme et al. (2018), (3) Zou et al. (2018), (4) Ranjan et al. (2020), (5) Ranjan et al. (2018), (6) Noterdaeme et al. (2007), (7) Kosenko & Balashev (2018), (8) Jorgenson et al. (2010), (9) Guimarães et al. (2012), (10) Noterdaeme et al. (2015).

(c) This work.

Table 2. Known HD-bearing DLA systems.

| Quasar | z_{em} | z_{abs} | $\log N(\text{HI})$ | $[\text{X}/\text{H}]^a$ | X | $\log N(\text{H}_2)$ | $N(\text{HD})$ | References ^b |
|-------------|-----------------|------------------|-------------------------|-------------------------|----|-------------------------|-------------------------|-------------------------|
| J 0000+0048 | 3.03 | 2.5255 | 20.8 ± 0.1 | 0.46 ± 0.45 | Zn | 20.43 ± 0.02 | $16.64^{+0.16}_{-0.18}$ | 1 |
| B 0120-28 | 0.434 | 0.18562 | 20.50 ± 0.10 | $-1.19^{+0.15}_{-0.21}$ | S | 20.00 ± 0.10 | 14.82 ± 0.15 | 2 |
| Q 0528-2505 | 2.77 | 2.81112 | 21.35 ± 0.10 | -0.68 ± 0.02 | Zn | 17.85 ± 0.02 | 13.33 ± 0.02 | 3, 4 |
| J 0643-5041 | 3.09 | 2.658601 | 21.03 ± 0.08 | -0.91 ± 0.09 | Zn | 18.54 ± 0.01 | 13.65 ± 0.07 | 5 |
| J 0812+3208 | 2.7 | 2.626443 | 21.35 ± 0.10 | -0.81 ± 0.10 | Zn | 19.93 ± 0.04 | 15.71 ± 0.07 | 6, 7 |
| | | 2.626276 | | -0.81 ± 0.10 | Zn | 18.82 ± 0.37 | 12.98 ± 0.22 | 6, 7 |
| J 0843+0221 | 2.92 | 2.786 | 21.82 ± 0.11 | $-1.52^{+0.08}_{-0.10}$ | Zn | 21.21 ± 0.02 | $17.35^{+0.15}_{-0.34}$ | 8 |
| J 1232+0815 | 2.57 | 2.3377 | $20.90^{+0.08}_{-0.10}$ | -1.32 ± 0.12 | S | $19.57^{+0.10}_{-0.13}$ | $15.53^{+0.17}_{-0.12}$ | 9, 10 |
| J 1237+0647 | 2.78 | 2.68959 | 20.00 ± 0.15 | 0.34 ± 0.12 | Zn | 19.20 ± 0.13 | 14.48 ± 0.05 | 11 |
| J 1331+170 | 2.08 | 1.77637 | 21.18 ± 0.04 | -1.22 ± 0.10 | Zn | 19.43 ± 0.10 | 14.83 ± 0.15 | 6, 12 |
| | | 1.77670 | | -1.22 ± 0.10 | Zn | 19.39 ± 0.11 | 14.61 ± 0.20 | 6, 12 |
| J 1439+1117 | 2.58 | 2.41837 | 20.10 ± 0.10 | 0.16 ± 0.11 | Zn | 19.38 ± 0.10 | 14.87 ± 0.03 | 13, 14 |
| J 2100-0641 | 3.14 | 3.09149 | 21.05 ± 0.15 | -0.73 ± 0.15 | Si | 18.76 ± 0.04 | 13.83 ± 0.06 | 15, 16 |
| J 2123-0050 | 2.261 | 2.0593 | 19.18 ± 0.15 | -0.19 ± 0.10 | S | 17.94 ± 0.01 | 13.87 ± 0.06 | 17 |
| J 2340-0053 | 2.083 | 2.05 | 20.35 ± 0.05 | -0.52 ± 0.06 | S | $18.62^{+0.02}_{-0.01}$ | 14.11 ± 0.06^c | 18 |

(a) Metallicity with respect to solar (Asplund et al. 2009): $[\text{X}/\text{H}] = \log(\text{X}/\text{H}) - \log(\text{X}/\text{H})_{\odot}$.

(b) References: (1) Noterdaeme et al. (2017), (2) Oliveira et al. (2014), (3) Klimenko et al. (2015), (4) Balashev et al. (2020), (5) Alborno Vázquez et al. (2014), (6) Balashev et al. (2010), (7) Jorgenson et al. (2009), (8) Balashev et al. (2017), (9) Ivanchik et al. (2010), (10) Balashev et al. (2011), (11) Noterdaeme et al. (2010), (12) Carswell et al. (2011), (13) Srianand et al. (2008), (14) Noterdaeme et al. (2008), (15) Ivanchik et al. (2015), (16) Jorgenson et al. (2010), (17) Klimenko et al. (2016), (18) Rawlins et al. (2018).

(c) This work.

3.1.3 J 0906+0548

We only tentatively detected HD absorption lines at the position of the main H₂ component ($z = 2.56918$) that has $\log N(\text{H}_2) = 18.87 \pm 0.02$ and $b = 6.8^{+0.1}_{-0.1} \text{ km s}^{-1}$. Although we did find HD lines at the expected positions, all of them are partially or fully blended with other absorption lines (see Fig. A3). Therefore, using z and priors on b obtained from

H₂ analysis, we were only able to place an upper limit to the HD column density in this component to be $\log N(\text{HD}) < 14.7$.

3.1.4 J0917+0154

This system was selected by [Ledoux et al. \(2015\)](#) in their search for cold gas at high redshift through C I lines. The detection and analysis of H₂ was presented by [Noterdaeme et al. \(2018\)](#) (they reported total column density $N(\text{H}_2) = 20.11 \pm 0.06$) and the metal lines were studied by [Zou et al. \(2018\)](#). Unfortunately, due to low resolution and relatively high velocity extent of H₂ lines, almost all HD lines are blended, including usually available L3-0R0, L4-0R0 and W0-0R0 lines. The only not blended line L0-0R0 has a very low oscillator strength and therefore we were able to put only very conservative upper limit on HD column density using priors on the redshifts and Doppler parameters for three components fit obtained from the refitting jointly C I and H₂ absorption lines. The fit to C I and HD lines are shown in Fig. A4 and H₂ lines profiles are presented in Fig. A17. The detailed fit result is given in Table A1.

3.1.5 J0946+1216

The detection of HD at the position of the main H₂ component ($z = 2.60642$, $\log N(\text{H}_2) = 19.96^{+0.01}_{-0.02}$, $b = 9.8^{+0.8}_{-0.3} \text{ km s}^{-1}$) for this system is also tentative. Unfortunately, the spectrum is very noisy and significantly contaminated by highly saturated H₂ lines and intervening Ly α forest absorption. Therefore we fixed z and used Doppler parameter from H₂ analysis as a prior. Hence we were only able to obtain relatively loose constraint on the HD column density in this component to be $\log N(\text{HD}) < 15.2$, see Fig. A5.

3.1.6 J1143+1420

This extremely saturated DLA at $z = 2.3228054$ was previously analysed by [Ranjan et al. \(2020\)](#) and H₂ column density was found to be $\log N(\text{H}_2) = 18.3 \pm 0.1$. We looked for HD lines associated with H₂, and we were able to place an upper limit on HD column density. We used fixed z and priors on Doppler parameter from H₂ analysis, and got $N(\text{HD}) < 15$. The fit to HD lines is shown in Fig. A6.

3.1.7 J1146+0743

We do not detected HD absorption lines at the position of both H₂ components ($z = 2.84163$ and 2.83946 with $N(\text{H}_2) = 18.76 \pm 0.01$ and $17.94^{+0.11}_{-0.13}$ respectively). Therefore we constrained $\log N(\text{HD}) < 14.4$ and $\log N(\text{HD}) < 14.5$ for the red and blue components, respectively, using a combination of HD L3-0R(0), HD L8-0R(0), HD W0-0R(0), HD W1-0R(0), HD L11-0R(0) and HD L12-0R(0) lines and priors on b and fixed z from H₂ analysis. The spectrum at the expected positions of HD absorption lines is shown in Fig. A7.

3.1.8 J1236+0010

We do not detect HD absorption lines at the position of H₂ component of DLA ($z = 3.03292$, $\log N(\text{H}_2) = 19.76 \pm 0.01$, $b = 2.3^{+0.2}_{-0.2} \text{ km s}^{-1}$). To fit HD lines we fixed z and used Doppler parameter of H₂ as a prior. Using HD L0-0R(0), HD L3-0R(0), HD L4-0R(0), HD L5-0R(0), HD W0-0R(0), HD L11-0R(0) and HD L14-0R(0) lines (see Fig. A8) we

put quite loose constraint on HD column density to be $\log N(\text{HD}) \lesssim 16.1$ since lines are found to be in the intermediate regime.

3.1.9 J1513+0352

The extremely saturated DLA at $z = 2.463598$ towards J1513+0352 was found in SDSS database by [Noterdaeme et al. \(2014\)](#). Detailed analysis of system by [Ranjan et al. \(2018\)](#) using X-shooter spectrum revealed a very high H₂ column density: $\log N(\text{H}_2) = 21.31 \pm 0.01$ (actually the highest value reported to the date at high- z). We detected HD L0-0R0, HD L5-0R0 and HD L7-0R0 absorption lines in this system. However, because of the H₂ lines were damped, they did not constrain the Doppler parameters. We therefore used instead the value obtained from associated C I as a prior for HD and obtained $\log N(\text{HD}) = 17.42^{+0.64}_{-1.09}$. This makes it the DLA with one of the highest HD column density as well. However, since the absorption lines are in the saturated regime and resolution is moderate, the uncertainty on $N(\text{HD})$ remains quite large. The fit to the HD absorption lines is shown in Fig. A9.

3.1.10 J2232+1242

We do not detect HD absorption lines in H₂-bearing DLA ($z = 2.2279378$, $N(\text{H}_2) = 18.56 \pm 0.02$, [Ranjan et al. 2020](#)) towards J2232+1242. Using redshift and prior on Doppler parameter from H₂ fit we obtain the upper limit on HD column density to be $\log N(\text{HD}) < 13.8$ (see Fig. A10).

3.1.11 J2347+0051

We detect HD absorption lines at the position of H₂ ($z = 2.58797$, $\log N(\text{H}_2) = 19.44 \pm 0.01$, $b = 6.2^{+0.2}_{-0.2} \text{ km s}^{-1}$). Using HD L3-0R(0), HD L5-0R(0), HD L7-0R(0), HD L13-0R(0) and HD L15-0R(0) lines (see Fig. A11), we measured HD column density to be $\log N(\text{HD}) = 14.33^{+0.18}_{-0.16}$ (to fit HD lines we fixed z and used prior on b from H₂ analysis).

3.2 KECK/HIRES and VLT/UVES data:

3.2.1 HE0027–1836

The extremely saturated DLA system at $z = 2.4018258$ have been studied by [Noterdaeme et al. \(2007\)](#); [Rahmani et al. \(2013\)](#). H₂ was identified in this DLA with column density $\log N(\text{H}_2) = 17.43$. Searching for HD absorption lines at the redshift of H₂ absorption lines, we obtained an upper limit on the HD column density $\log N(\text{HD}) < 13.6$ (we fixed z and used Doppler parameter as a prior from H₂ analysis) due to inconsistency of L2-0R0 and L3-0R0 lines with the fit in the spectrum (see Fig. A12).

3.2.2 J0812+3208

The spectrum towards J0812+3208 features two DLAs at $z = 2.626491$ and $z = 2.06779$ ([Prochaska et al. 2003](#)). [Jorgenson et al. \(2010\)](#) detected absorption lines from C I fine-structure levels in both of them. Associated HD/H₂ absorption lines at $z = 2.626491$ were studied in details by several

authors (Jorgenson et al. 2009; Balashev et al. 2010; Tumlinson et al. 2010), however, no significant attention have been paid to the system at $z = 2.06678$. Knowing that C I is an excellent tracer of H₂ in ISM (Noterdaeme et al. 2018), we searched for H₂ and HD molecules in this system as well. We used the Keck/HIRES spectrum whose reduction is detailed in Balashev et al. (2010). We detected H₂ absorption lines from $J \leq 4$ rotational levels, which we fitted using a one component model, with tied redshifts and Doppler parameter rotational levels for all levels. Indeed, H₂ lines are located at the blue end of the spectrum, covering only one-two unblended H₂ lines from each rotational level. The fit results is given in Table A2 and line profiles are shown in Fig. A18. Using relative population of $J = 1$ and $J = 0$ levels, we found the excitation temperature to be $T_{01} = 67^{+4}_{-3}$ K.

Unfortunately, only two HD lines (L0-0R0 and L1-0R0) were covered in this spectra and only the weakest HD L0-0R0 line from this system was unblended (see Fig. A18). Thus, we estimated only an upper limit to the HD column density, fixing the redshift and Doppler parameter from H₂, and obtained $\log N(\text{HD}) < 14.4$.

3.2.3 J 0816+1446

The multicomponent H₂-bearing DLA system towards J 0816+1446 was identified by Guimarães et al. (2012). This system have quite large redshift and hence is significantly blended with Ly α forest lines. Guimarães et al. (2012) reported H₂ in two components, with one at $z = 3.28742$ indicates a significantly high H₂ column density, $\log N(\text{H}_2) = 18.66 \pm 0.27$ to be searched for HD. We refit H₂ absorption lines at $z = 3.28742$ with three subcomponents, since it provides a better fit, and measured the total $\log N(\text{H}_2) = 18.51 \pm 0.04$ in agreement with Guimarães et al. (2012). Unfortunately, all HD lines are blended and therefore using fixed z and Doppler parameter from H₂ analysis we were able to obtain an upper limits on the HD column densities $\log N(\text{HD}) \lesssim 15$ from the L4-0 R(0) line (fit results are presented in Table A3 and Fig. A13).

3.2.4 J 1311+2225

This multicomponent H₂-bearing DLA system was selected through C I by Ledoux et al. (2015). Noterdaeme et al. (2018) reported $\log N(\text{H}_2) = 19.69 \pm 0.01$ in this system, using single component model, but they noted that four components for H₂ lines can be distinguished. We refitted H₂ and C I lines in this system using four-component model. First we fit C I absorption lines from three fine-structure levels, where we tied Doppler parameters for each component. Then we performed a four-component fit to the H₂ lines, where the selection of initial guess of components was based on C I result. For H₂, we tied Doppler parameters only between $J = 0$ and $J = 1$ levels, while Doppler parameters for other rotational levels were allowed to vary independently. However, since the components are significantly blended among themselves and the data is quite noisy, we added two penalty functions to the likelihood. The first one is set to artificially suppress situations where the Doppler parameter of the some J level would be lower than that of the $J - 1$ level. This is well motivated physically and observationally, since the increase of

the Doppler parameters for the higher H₂ rotational levels has been established in many H₂ absorption systems (see e.g. Lacour et al. 2005; Noterdaeme et al. 2007; Balashev et al. 2009). The other penalty is to keep a reasonable excitation diagram of H₂: we penalized models with $T_{J-1,J} > T_{J,J+1}$ ⁴. This is also reasonably motivated by both observations and modelling (see e.g. Klimenko & Balashev 2020). Therefore we get total H₂ column density to be $N(\text{H}_2) = 19.59 \pm 0.01$, which is a bit lower than the value 19.69 ± 0.01 reported previously (Noterdaeme et al. 2018). The fitting results are shown in Table A4 and C I and H₂ profiles in Figs. A19, A20, A21, A22, A23.

We also estimated metallicity in this system. Unfortunately, very few metal lines, that are usually used to obtain metallicity, were covered in this spectrum, and almost all covered lines are blended. Therefore to obtain metallicity we used Zn II 2062 line. We fitted this line, assuming 4 components in the positions of C I components, and obtained Zn II total column density to be $12.84^{+0.09}_{-0.11}$, therefore the metallicity is $-0.34^{+0.13}_{-0.14}$ relative to solar. The fit to Zn II absorption line is shown in Fig. A24.

We again used a four-component model to analyse HD, associated with C I components. We found that component 3 for HD is shifted in comparison with C I lines. However, the component 3 in C I have quite large Doppler parameter, that indicates that there is velocity structure within this component, which meanwhile we can not resolve due to low quality of the spectrum and mutual blending from other components. So for HD we did not use the H₂ and C I priors on redshifts (except weak component 1, where only upper limit on HD column density could be placed) and Doppler parameters. After MCMC procedure we found HD to be detected in the component 2, 3 and 4, and the redshifts of the components are well agree within uncertainties (see Table A4). Component 1 is too weak, so we could only place an upper limit on $N(\text{HD})$ there. The fit to the HD lines is shown in Fig. A14 and HD column densities reported in Table A4.

3.2.5 J 2140-0321

H₂ absorption lines were previously found and analysed by Noterdaeme et al. (2015); Ranjan et al. (2020) at $z = 2.339$ and H₂ column density was found to be quite large $\log N(\text{H}_2) = 20.13$. To fit HD absorption lines we used together the spectra, obtained by X-shooter and UVES. However, since the UVES spectrum is very noisy, and X-shooter is low-resolution hence it is not appropriate for HD analysis. Therefore we were able only to place upper limit on HD column density to be $\log N(\text{HD}) < 14.6$ using the priors on the Doppler parameters and the redshifts obtained from H₂ analysis (Noterdaeme et al. 2015), see Fig. A15.

3.2.6 J 2340-0053

C I and H₂ absorption lines in the DLA at $z \approx 2.055$ towards J 2340-0053 were first reported by Jorgenson et al. (2010).

⁴ where $T_{J,J+1}$ is the excitation temperature between J and $J+1$ levels

These authors found C I in nine components, while they fitted H₂ using a six components model. This spectrum was recently reanalysed by [Rawlins et al. \(2018\)](#) with a seven components for both C I and H₂ and found their redshifts to be consistent with each other. HD absorption lines, associated with H₂ were later independently detected by [Kosenko & Balashev \(2018\)](#) and [Rawlins et al. \(2018\)](#). In this paper, we present detailed reanalysis of HD, H₂ and C I absorption lines.

Using the reduced 1D-spectrum of J2340–0053 from the KODIAQ database ([O’Meara et al. 2017](#)), we refitted C I, H₂ and HD absorption lines with seven component model using the same methodology as in the previous section for J1311+2225. We fit C I lines first, taking into account the partial coverage of the background emission line region by C I line at $\sim 1560\text{\AA}$ reported by [Bergeron & Boissé \(2017\)](#). We fit the covering factors as an independent parameter following the methodology from [Balashev et al. \(2011\)](#). We found that a fit with three independent covering factors for each of the three main components provides a better fit, than using a single covering factor for all components. We then used the C I fit as first guess to the redshifts of the H₂ lines. Unfortunately, three central components are significantly blended with each other in almost all H₂ absorption lines from $J = 0, 1, 2$ and 3 rotational levels. Therefore we used redshifts determined during C I fit as priors, and as for J1311+2225, we used penalty functions during H₂ analysis to reproduce physically reasonable constraints. We obtained the total H₂ column density to be $\log N(\text{H}_2) = 18.57 \pm 0.02$, which is higher than reported by ([Rawlins et al. 2018](#), $\log N(\text{H}_2) = 17.99 \pm 0.05$). The difference is partly due to the fact that [Rawlins et al. \(2018\)](#) tied all H₂ Doppler parameters for $J > 0$ to H₂ $J = 0$, while we tied only H₂ $J = 1$ and allowed increasing b -values for other levels. The fitting results are shown in Table A5 and C I and H₂ profiles in Figs A25, A26, A27, A28.

We fit HD absorption lines at the positions of these components using the priors on the Doppler parameters from the fit of $J = 0$ and $J = 1$ rotational levels of H₂. However, the exact b -values affect little the results since the HD absorption lines are optically thin. The obtained total HD column density is $\log N(\text{HD}) = 14.11 \pm 0.06$, which is a bit lower than found by [Rawlins et al. \(2018\)](#) ($\log N(\text{HD}) = 14.28 \pm 0.08$). The fit to the HD lines is reported in Table A5 and shown in Fig. A16.

4 RESULTS

We summarize our new measurements of HD (and H₂) column densities and relative abundance of $N(\text{HD})/2N(\text{H}_2)$ in Table 3. In total, we report four new detections of HD molecules in high-redshift DLAs (sometimes in several components) and place upper-limits for another twelve.

Fig. 1 compares the HD and H₂ column densities in the Galaxy ([Snow et al. 2008](#)) and at high redshift (new measurements and values from Table 2). We also compare the data to the primordial D/H isotopic ratio derived from updated Big Bang Nucleosynthesis (BBN) calculations ([Pitrou et al. 2018](#)) and $\Omega_b h^2$ from ([Planck Collaboration et al. 2020](#)). One can see that the molecular ratios are well below the primordial isotopic ratio in the Galaxy, while distant

measurements do not show such a tendency and instead indicate a systematically higher HD/H₂ relative abundance than locally at specific $\log N(\text{H}_2)$, and closer to the BBN value.

Several processes can in principle affect the HD/H₂ relative abundance, such as fractionation and astration of deuterium. The chemical fractionation of D (the process through which D efficiently replaces hydrogen in complex molecules, such as D₂, HDO, D₂O, NH₂D, NHD₂, ND₃, H₂D⁺, DCO⁺, etc.) should play a minor role, since complex molecules mainly reside in the cold dense medium with $n_{\text{H}} \gtrsim 10^5 \text{ cm}^{-3}$ and $T \lesssim 25 \text{ K}$ (see e.g. [Kim et al. 2020](#), and references therein), which is not the case here as we probe more diffuse clouds. Measurements at high z tend to probe lower metallicities than locally and hence represent gas that has been less processed in stars. Such gas should therefore be less affected by astration of deuterium than measurements in the Galaxy (i.e. $\sim 10 \text{ Gyr}$ later). However, [Dvorkin et al. \(2016\)](#) showed that D/H is never reduced to less than 1/3 of its primordial ratio, i.e. astration cannot explain the observed discrepancy. On the other hand, the low metallicity affects the HD abundance from the chemical pathway ([Liszt 2015](#); [Balashev & Kosenko 2020](#)). Indeed, as the metallicity decreases, both the dust abundance and electron fraction comes from carbon (here we consider diffuse in the diffuse ISM) decrease. This results in a drop of the radiative and H⁺ grain recombination rates, and hence the ionization fraction of H and D increases (see set of reactions leading to HD, 1). This then results in an increase of the HD formation rate through the reaction:



The enhanced HD formation rate consequently increases the HD abundance relative to H₂. Interestingly, in certain physical conditions, this may lead to a D/HD transition occurring earlier (lower penetration depth) in ISM clouds than the H/H₂ transition ([Balashev & Kosenko 2020](#)). The evident observational consequence of this is that $N(\text{HD})/2N(\text{H}_2) > \text{D}/\text{H}$, while the opposite case was generally assumed (e.g. [Le Petit et al. 2002](#)), since naively HD is always significantly less self-shielded in the medium than H₂. In conclusion, the typically lower metallicities at high z can in principle explain the systematic difference in relative HD/H₂ abundance between high- z and Milky-Way measurements (see also [Liszt 2015](#)).

5 PHYSICAL CONDITIONS

The relative HD/H₂ abundance depends not only on the metallicity, but also on the physical conditions in the medium – number density, UV flux, and cosmic-ray ionization rate ([Le Petit et al. 2002](#); [Ćirković et al. 2006](#); [Liszt 2015](#)). To describe this dependence, we used recently published simple semi-analytic description of the dependence of the HD/H₂ ratio on these parameters ([Balashev & Kosenko 2020](#)). This method includes solving the HD balance equation between formation and destruction processes in a plane-parallel, steady-state cloud and permits the determination of how $N(\text{HD})$ – as a function of $N(\text{H}_2)$ – depends on the physical properties in the cloud, namely cosmic-ray ionization rate per hydrogen atom (CRIR, ζ), UV field intensity

Table 3. Results from the analysis of HD lines.

| Quasar | z | b (km s $^{-1}$) | $\log N(\text{HD})^a$ | $\log N(\text{H}_2)$ | $N(\text{HD})/2N(\text{H}_2)$ |
|--------------------------|-----------------------------|----------------------|-------------------------|-------------------------|---------------------------------------|
| X-shooter data: | | | | | |
| J 0136+0440 | 2.779430 | $7.7^{+2.4}_{-1.9}$ | < 14.5 | $18.64^{+0.06}_{-0.08}$ | $< 3.6 \times 10^{-5}$ |
| J 0858+1749 | 2.625241 | $7.9^{+0.4}_{-0.4}$ | $14.87^{+0.06}_{-0.09}$ | $19.72^{+0.01}_{-0.02}$ | $(7.1^{+1.1}_{-1.4}) \times 10^{-6}$ |
| J 0906+0548 | 2.569180 | $6.8^{+0.1}_{-0.1}$ | < 14.7 | $18.87^{+0.02}_{-0.02}$ | $< 3.4 \times 10^{-5}$ |
| J 0917+0154(b) | 2.10586 | $5.2^{+1.1}_{-1.8}$ | < 12 | $17.96^{+0.82}_{-0.16}$ | $< 5.5 \times 10^{-7}$ |
| | 2.10624 | $6.4^{+1.5}_{-2.4}$ | < 15.9 | $18.4^{+1.0}_{-0.3}$ | $< 1.6 \times 10^{-3}$ |
| | 2.106812 | $4.7^{+1.1}_{-1.3}$ | < 18.1 | $20.09^{+0.07}_{-0.08}$ | $< 5.1 \times 10^{-3}$ |
| J 0946+1216 | 2.606406 | $9.8^{+0.8}_{-0.3}$ | < 15.2 | $19.96^{+0.01}_{-0.02}$ | $< 9.0 \times 10^{-6}$ |
| J 1143+1420 | 2.3228054 | $2.2^{+2.0}_{-0.1}$ | < 15 | $18.3^{+0.1}_{-0.1}$ | $< 2.5 \times 10^{-4}$ |
| J 1146+0743 | 2.839459 | $7.6^{+0.6}_{-0.4}$ | < 14.5 | $17.94^{+0.11}_{-0.13}$ | $< 1.8 \times 10^{-4}$ |
| | 2.841629 | $11.4^{+0.5}_{-0.7}$ | < 14.4 | $18.76^{+0.01}_{-0.01}$ | $< 2.2 \times 10^{-5}$ |
| J 1236+0010 | 3.03292 | $2.3^{+0.2}_{-0.2}$ | < 16.1 | $19.76^{+0.01}_{-0.01}$ | $< 1.1 \times 10^{-4}$ |
| J 1513+0352 | 2.463598 | $3.9^{+0.3}_{-0.3}$ | $17.42^{+0.64}_{-1.09}$ | $21.31^{+0.01}_{-0.01}$ | $(6.4^{+2.1}_{-5.9}) \times 10^{-5}$ |
| J 2232+1242 | 2.2279378 | $8.1^{+1.1}_{-1.2}$ | < 13.8 | $18.56^{+0.02}_{-0.02}$ | $< 8.7 \times 10^{-4}$ |
| J 2347+0051 | 2.587971 | $6.2^{+0.2}_{-0.2}$ | $14.33^{+0.18}_{-0.16}$ | $19.44^{+0.01}_{-0.01}$ | $(3.9^{+2.0}_{-1.2}) \times 10^{-6}$ |
| High-resolution data: | | | | | |
| HE 0027–1836 | 2.4018258 | $1.2^{+0.1}_{-0.2}$ | < 13.6 | $17.43^{+0.02}_{-0.02}$ | $< 7.4 \times 10^{-5}$ |
| J 0812+3208 | $2.066780^{(+1)}_{(-1)}$ | $4.4^{+0.1}_{-0.1}$ | < 14.4 | $19.26^{+0.02}_{-0.01}$ | $< 7.4 \times 10^{-6}$ |
| J 0816+1446(b) | $3.287252^{(+3)}_{(-2)}$ | $0.6^{+0.1}_{-0.1}$ | < 14.9 | $16.97^{+0.09}_{-0.10}$ | $< 4.3 \times 10^{-3}$ |
| | $3.287399^{(+2)}_{(-3)}$ | $1.5^{+0.1}_{-0.1}$ | < 14 | $18.43^{+0.04}_{-0.03}$ | $< 1.9 \times 10^{-5}$ |
| | $3.287515^{(+2)}_{(-3)}$ | $1.1^{+0.1}_{-0.1}$ | < 14.2 | $17.60^{+0.10}_{-0.10}$ | $< 2.0 \times 10^{-4}$ |
| J 1311+2225 | $3.091410^{(+21)}_{(-14)}$ | $8.0^{+4.6}_{-5.4}$ | < 12.8 | $17.87^{+0.37}_{-0.33}$ | $< 4.4 \times 10^{-6}$ |
| | $3.0915397^{(+66)}_{(-77)}$ | $5.4^{+0.8}_{-0.8}$ | $14.82^{+0.08}_{-0.08}$ | $19.52^{+0.02}_{-0.02}$ | $(1.0^{+0.3}_{-0.2}) \times 10^{-5}$ |
| | $3.091714^{(+28)}_{(-48)}$ | $\lesssim 2.8$ | $14.30^{+0.37}_{-0.31}$ | $18.25^{+0.22}_{-0.39}$ | $(5.6^{+13.7}_{-3.2}) \times 10^{-5}$ |
| | $3.091871^{(+11)}_{(-26)}$ | $4.0^{+1.6}_{-1.2}$ | $14.27^{+0.10}_{-0.13}$ | $18.57^{+0.05}_{-0.09}$ | $(2.5^{+0.9}_{-0.7}) \times 10^{-6}$ |
| Total: | | | $15.02^{+0.11}_{-0.07}$ | $19.59^{+0.01}_{-0.01}$ | $(1.3^{+0.4}_{-0.2}) \times 10^{-5}$ |
| J 2140–0321 | $2.33996^{(+3)}_{(-3)}$ | $4.5^{+0.9}_{-0.7}$ | < 14.6 | $20.13^{+0.07}_{-0.07}$ | $< 1.5 \times 10^{-6}$ |
| J 2340–0053 ^b | $2.0541703^{(+6)}_{(-4)}$ | $2.5^{+0.1}_{-0.1}$ | < 13.5 | $15.99^{+0.04}_{-0.04}$ | $< 1.7 \times 10^{-3}$ |
| | $2.0542913^{(+4)}_{(-9)}$ | $1.7^{+0.1}_{-0.2}$ | < 12.7 | $15.24^{+0.04}_{-0.03}$ | $< 1.4 \times 10^{-3}$ |
| | $2.054528^{(+3)}_{(-3)}$ | $3.0^{+0.1}_{-0.2}$ | < 13.8 | $17.11^{+0.12}_{-0.14}$ | $< 2.2 \times 10^{-4}$ |
| | $2.054610^{(+1)}_{(-1)}$ | $1.0^{+0.1}_{-0.3}$ | $13.60^{+0.15}_{-0.14}$ | $18.27^{+0.06}_{-0.06}$ | $(1.1^{+0.5}_{-0.3}) \times 10^{-5}$ |
| | $2.054723^{(+3)}_{(-3)}$ | $3.1^{+0.1}_{-0.1}$ | $13.84^{+0.05}_{-0.05}$ | $18.14^{+0.04}_{-0.04}$ | $(2.5^{+0.4}_{-0.3}) \times 10^{-5}$ |
| | $2.0549952^{(+5)}_{(-4)}$ | $3.8^{+0.1}_{-0.1}$ | < 12.6 | $16.43^{+0.03}_{-0.03}$ | $< 7.1 \times 10^{-5}$ |
| | $2.0551398^{(+6)}_{(-4)}$ | $1.8^{+0.1}_{-0.1}$ | $13.29^{+0.15}_{-0.21}$ | $17.43^{+0.04}_{-0.05}$ | $(3.6^{+1.6}_{-0.3}) \times 10^{-5}$ |
| Total: | | | $14.11^{+0.06}_{-0.06}$ | $18.57^{+0.02}_{-0.02}$ | $(1.7^{+0.3}_{-0.2}) \times 10^{-5}$ |

(a) The point and interval estimates were obtained from a 1D marginalized posterior distribution function, and correspond to its maximum and 0.683 (1 σ) confidence interval, respectively. In case of tentative detection, the upper limits are constrained from the 1 σ one-sided confidence interval.

(b) These system were re-fitted to get consistent results for HD, H₂, and C I (see text).

(relative to Draine field, [Draine 1978](#), χ), number density ($n = n_{\text{H I}} + 2n_{\text{H}_2}$), and metallicity (Z). We assumed that the D/H isotopic ratio is 2.5×10^{-5} for all systems, i.e., we neglected a possible astration of D, which is typically much smaller ([Dvorkin et al. 2016](#)) than the uncertainties of this method (see below).

To constrain the distributions of the physical parameters from the measured $N(\text{HD})$ and $N(\text{H}_2)$, we followed a Bayesian approach using affine-invariant Markov Chain Monte Carlo (MCMC) sampling ([Foreman-Mackey et al. 2013](#)). Because we don't have access to the total hydrogen ($N(\text{H I}) + N(\text{H}_2)$) in individual HD-bearing components, the metallicity for each cloud was set to the overall metallicity in the corresponding DLA, as provided in Tables 1 and

2. For the intensity of the UV field as well as the number density, we used priors that have been estimated from the analysis of the relative population of H₂ rotational and C I fine-structure levels ([Balashev et al. 2019](#); [Klimenko & Balashev 2020](#)). This allows us to significantly reduce the constrained probability distribution function of CRIR, for which we used a flat prior on $\log \zeta$. An example of the constrained 1D and 2D-posterior probability distribution functions of the parameters for the system towards J 0858+1749 is given in Fig. 2. The derived physical conditions for the sample are summarised in Table 4, and plots of the marginalized posterior distribution functions for each component are shown in Figures B1 – B5. We do not report results for J 1513+0352 nor J 1311+2225 (component 3), towards which we obtained

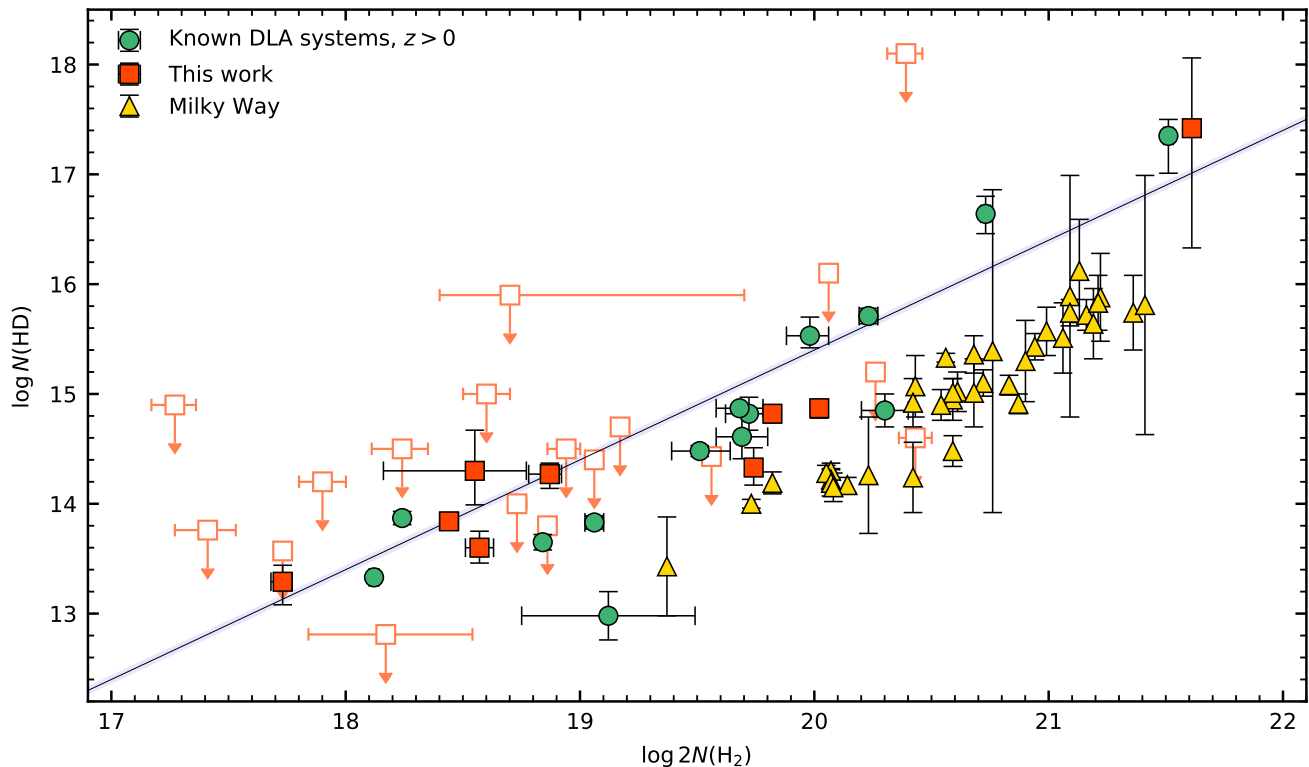


Figure 1. Relative abundance of HD and H₂ molecules. Green circles, red squares, and yellow triangles correspond to known HD-bearing systems at high redshift (for references, see text), new HD detections at high redshift and upper limits on HD column densities (filled and empty squares; this work), and measurements in the Galaxy (Snow et al. 2008), respectively. The solid blue line shows the D/H isotopic ratio estimated using standard BBN calculations and $\Omega_b h^2$ from the Planck Collaboration et al. (2020).

a very loose constraint on ζ , due to large uncertainties on the HD column densities. Note that the constraints on the number density, n , and UV flux, χ , typically match the priors used.

6 DISCUSSION

We find the CRIRs to vary significantly from $\zeta \sim 10^{-18}$ to 10^{-15} s^{-1} , possibly reflecting a wide range of environments being probed by our sample. Indeed, DLA systems are selected owing to their absorption cross-section and likely probe the overall galaxy population, with a high fraction of low-mass galaxies at high redshift (e.g., Cen 2012), in which the star-formation and cosmic-ray ionization rates are expected to vary significantly. Even though the HD/H₂ absorption systems in our sample do not necessarily probe the immediate environments of star formation, as we will show below, the measured high CRIR values correlate with the relatively high UV fluxes that reach up to 10 times the Draine field.

We find that the range of CRIR estimates are in line with other recent measurements both at high redshift (Indriolo et al. 2018; Muller et al. 2016; Shaw et al. 2016) and in nearby galaxies (van der Tak et al. 2016; González-Alfonso et al. 2013, 2018), which also show quite large dispersion. This dispersion can be partly due to the use of various methods, or connected to a real physical dispersion of the

CRIR. Indeed, the measurements in the Galaxy (for a review see Padovani et al. 2020, and references therein) and in the lensed system at $z \sim 0.89$ towards PKS 1830–211 (Muller et al. 2016) show that this parameter can vary significantly between different sightlines even inside a given galaxy, mostly depending on the proximity to the CR accelerator. Le Petit et al. (2016) also present evidence of CRIR enhancement in the center of the Galaxy relative to the disk. Finally, we think that the comparison of previous data with our measurement is likely not straightforward since different methods have been used, which probe various environments. Indeed, the aforementioned and most recent constraints on CRIR in local and high- z galaxies have been based on oxygen-bearing species (OH^+ and H_2O^+). Since these have been analysed in quite luminous starburst galaxies with roughly solar metallicity and high star formation rates, they may sample rather high CRIR values compared to the overall galaxy population.

Figure 3 shows and compares our measurements with literature ones in the $[\zeta, \log N(\text{H}_2)]$ plane. An attenuation of the cosmic-ray ionization rate with increasing column density is theoretically expected (Padovani et al. 2009). However, we do not see strong evidence for a correlation between ζ and $N(\text{H}_2)$ in our sample, probably because of the large dispersion (unweighted Pearson test gives correlation coefficient $r = -0.49$, with p-value 0.08). In addition, we probe mostly diffuse clouds with low cloud depths (except Q 0843 + 0221 which will be discussed later), which may

Table 4. Constraints on physical conditions.

| Quasar | $\log \zeta$ | $\log \chi$ | $\log n$ | Ref. [†] |
|-----------------|-----------------------|----------------------|---------------------|-------------------|
| J 0000+0048 | $\gtrsim -16.3$ | $0.0^{+0.3}_{-0.3}$ | $1.2^{+0.5}_{-0.4}$ | (2) |
| Q 0528-2505 | $-14.9^{+0.2}_{-0.1}$ | $1.1^{+0.1}_{-0.1}$ | $2.4^{+0.1}_{-0.1}$ | (3) |
| J 0812+3208, c1 | $-16.6^{+1.4}_{-0.5}$ | $-0.1^{+0.2}_{-0.1}$ | $2.4^{+0.2}_{-0.2}$ | (2) |
| J 0812+3208, c2 | $\lesssim -19.2$ | $-0.8^{+0.2}_{-0.2}$ | $0.8^{+0.3}_{-0.3}$ | (2) |
| J 0843+0221 | $-16.5^{+0.9}_{-1.1}$ | $2.0^{+0.1}_{-0.1}$ | $1.9^{+0.1}_{-0.1}$ | (2) |
| J 0858+1749 | $-17.3^{+0.1}_{-0.1}$ | $0.1^{+0.2}_{-0.2}$ | $1.8^{+0.1}_{-0.1}$ | (1) |
| J 1232+0815 | $-18.3^{+0.3}_{-0.3}$ | $-0.4^{+0.2}_{-0.2}$ | $1.6^{+0.1}_{-0.1}$ | (2) |
| J 1237+0647 | $-14.8^{+0.2}_{-0.2}$ | $1.1^{+0.1}_{-0.1}$ | $1.3^{+0.1}_{-0.1}$ | (2) |
| J 1311+2225, c2 | $-16.2^{+0.1}_{-0.1}$ | $1.1^{+0.1}_{-0.1}$ | $1.7^{+0.2}_{-0.2}$ | (4) |
| J 1311+2225, c3 | — | $1.0^{+0.1}_{-0.1}$ | $1.9^{+0.1}_{-0.1}$ | (4) |
| J 1311+2225, c4 | $-15.1^{+0.2}_{-0.3}$ | $0.6^{+0.2}_{-0.2}$ | $2.1^{+0.3}_{-0.2}$ | (4) |
| J 1439+1118 | $-15.4^{+0.3}_{-0.2}$ | $0.8^{+0.2}_{-0.2}$ | $0.9^{+0.2}_{-0.2}$ | (2) |
| J 1513+0352 | — | $0.6^{+0.3}_{-0.2}$ | $1.9^{+0.1}_{-0.2}$ | (2) |
| J 2100-0641 | $-17.2^{+0.3}_{-0.2}$ | $-0.3^{+0.3}_{-0.3}$ | $1.4^{+0.3}_{-0.3}$ | (2) |
| J 2340-0053, c4 | $-16.4^{+0.7}_{-0.7}$ | $-0.1^{+0.2}_{-0.3}$ | $0.6^{+0.3}_{-0.4}$ | (4) |
| J 2340-0053, c5 | $-14.8^{+0.2}_{-0.2}$ | $0.6^{+0.1}_{-0.1}$ | $1.2^{+0.1}_{-0.1}$ | (4) |
| J 2340-0053, c7 | $-15.4^{+0.8}_{-1.0}$ | $-0.2^{+0.2}_{-0.2}$ | $0.8^{+0.4}_{-0.4}$ | (4) |
| J 2347+0051 | $-17.6^{+0.6}_{-0.5}$ | $-0.4^{+0.4}_{-0.4}$ | $2.8^{+0.1}_{-0.1}$ | (1) |

[†] References used to obtain priors on χ and n : (1) Balashev et al. (2019), (2) Klimenko & Balashev (2020), (3) Balashev et al. (2020), (4) this work.

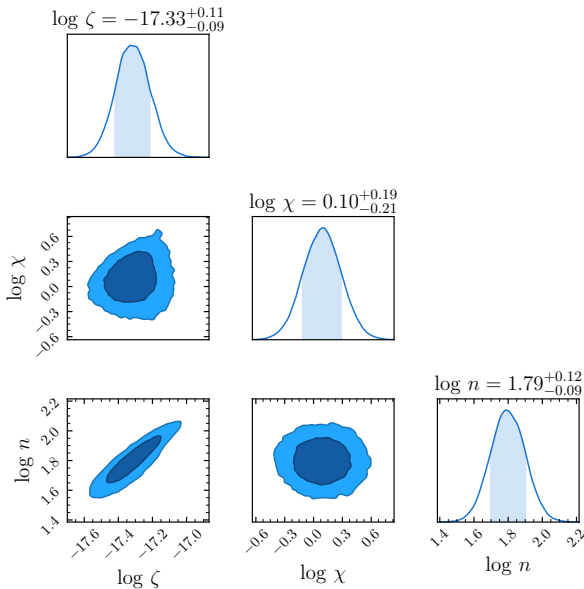


Figure 2. Posterior probability functions for CRIR (ζ), UV field intensity (χ), and number density (n) obtained from HD/H₂ fitting for the system at $z = 2.625241$ towards J0858+1749. The diagonal panels show 1D marginalized posterior function, non-diagonal show 2D posterior functions, where the dark- and light-blue regions correspond to 1σ and 2σ confidence levels, respectively.

be insufficient to attenuate the cosmic-ray flux. Additionally, the observed clouds should have quite large ($N(\text{HI}) \gtrsim 10^{20} \text{ cm}^{-2}$) column densities of associated H I, which is hard to constrain observationally, but which is also able to attenuate the CR flux, and therefore may provide an additional uncertainty in our calculations.

Previous measurements at high redshift and in the Galaxy show that in case of a denser medium (e.g., dense cores, blue triangles, Caselli et al. (1998) and protostellar envelopes, light green triangles, for references see Padovani et al. (2009)) the cosmic-ray ionization rates tend to be slightly lower.

In Figure 4, we investigate the dependence of ζ on the intensity of the UV field, number density and metallicity in the medium. The CRIR is found to correlate strongly with the UV field intensity, while it does not correlate with number density and only slightly correlates with metallicity. Removing a possible outlier at $\log \chi \sim 2$ (corresponding to J0843+0221) and lower and upper limits from J0000+0048 and J0812+3208 (comp 2), we find a Pearson correlation coefficient between ζ and χ of $r = 0.75$ (with p-value=0.002 to reject the null hypothesis that ζ and χ do not correlate). The outlier in this plot (J0843+0221) may be due to its very high H₂ column density, with suppression of the CRIR or due to its exceptionally low metallicity.

Indeed, in our formalism, we assume CRIR, ζ , to be constant throughout the cloud. However, it is expected that CRIR can be attenuated in the cloud at column densities $N(\text{H}) \gtrsim 10^{20} \text{ cm}^{-2}$ (see, e.g., Silsbee & Ivlev 2019). Therefore, if the CRIR is attenuated inside the cloud, then the derived value of ζ is lower than the incident value. That means that in principle, to draw accurate physical conclusions, cosmic-ray propagation effects at high column densities should be taken into account properly. This would also require knowledge of the magnetic-field configuration in DLAs, which is not well probed by available observations.

Since the relative HD/H₂ abundance depends in opposite ways on ζ and χ (i.e., $N(\text{HD})/N(\text{H}_2)$ increases when ζ increases but also when χ decreases), the ζ - χ correlation could be artificially introduced by issues in the measurements themselves. However, the posterior distributions for individual systems (e.g., Fig 2) indicate that the measurements of ζ may correlate more strongly with n than with χ (if any). We also note that the HD/H₂ ratio depends on the number density and metallicity (with similar sensitivity on variation of n as for χ , and even higher sensitivity for metallicity (see Balashev & Kosenko 2020); therefore, it is not evident why we should see a strong correlation between ζ and χ , and a lack of correlation between ζ and n . This motivates us to assume that the ζ - χ correlation has a real physical origin.

Indeed, we expect a common star-formation origin between cosmic rays and UV radiation. Furthermore, one can see that the slope of the $\log \zeta - \log \chi$ correlation is close to 2, i.e., CRIR increases quadratically with the strength of the UV field. This also may have reasonable explanation, since the low-energy cosmic rays ($\lesssim 100$ MeV, that mostly determine the ionization rate) may have complex propagation behaviour, related to the diffusion in the ISM magnetic fields. In addition, taking into account the energy losses (see loss function for cosmic rays in Padovani et al. 2018), this may result in a local enhancement of the ζ/χ ratio near the production sites and hence super-linear dependence of ζ on χ , since UV photons escape much more easily from the star-forming regions.

Assuming that $\zeta \propto \chi^2$ dependence is real, we plot the $\sqrt{\zeta}/\chi$ as a function of $\log N(\text{H}_2)$ in Fig. 5. One can see that indeed for the main bulk of the systems with $\log N(\text{H}_2)$ in

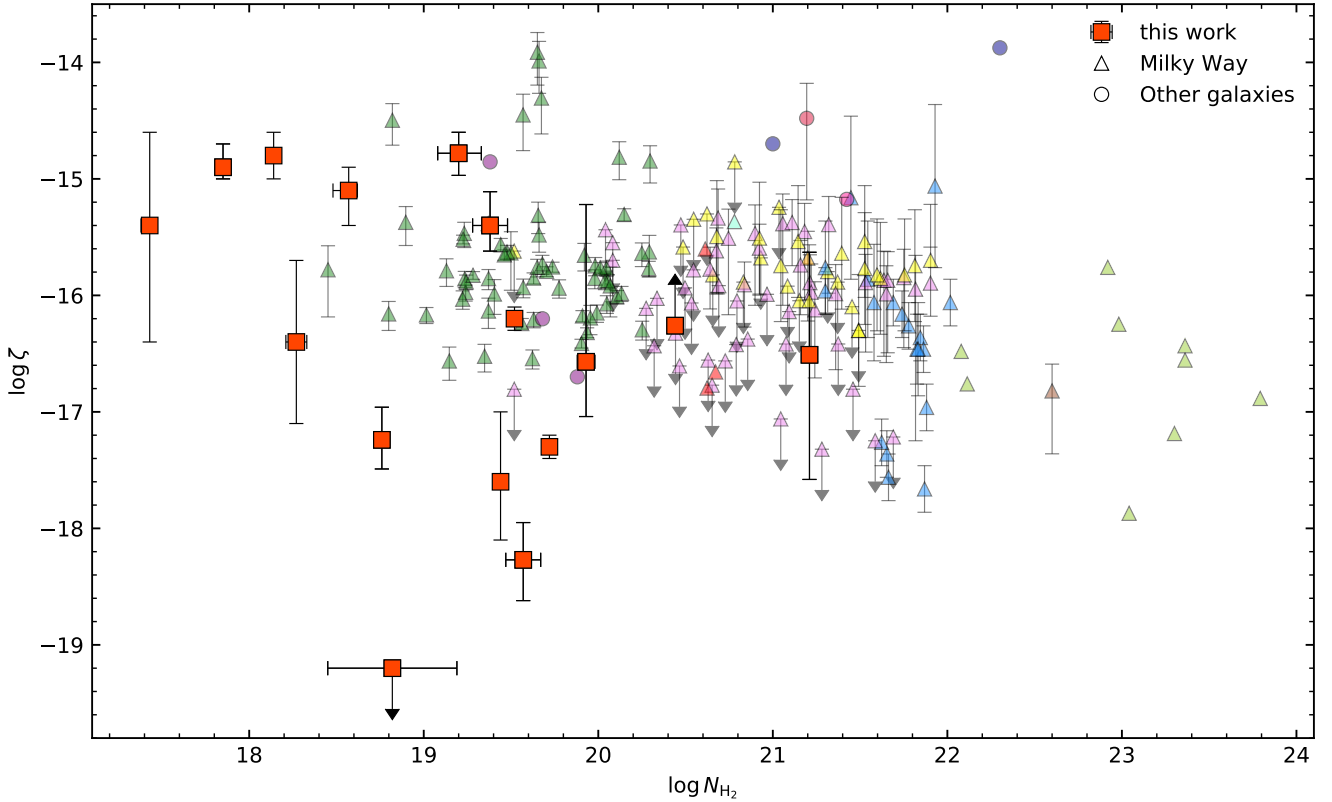


Figure 3. Estimated CRIR as a function of H_2 column density. Here, red squares are values obtained in this work, smaller squares are values obtained for other galaxies (blue - Muller et al. (2016); violet - Shaw et al. (2016); pink - Indriolo et al. (2018)), triangles are values measured in the Galaxy (yellow - Indriolo et al. (2007); light green are protostellar envelopes (for references, see table 6 from Padovani et al. 2009); blue - Caselli et al. (1998); cyan - Shaw et al. (2008); brown - Maret & Bergin (2007); violet - Indriolo & McCall (2012); dark green - Indriolo et al. (2015)).

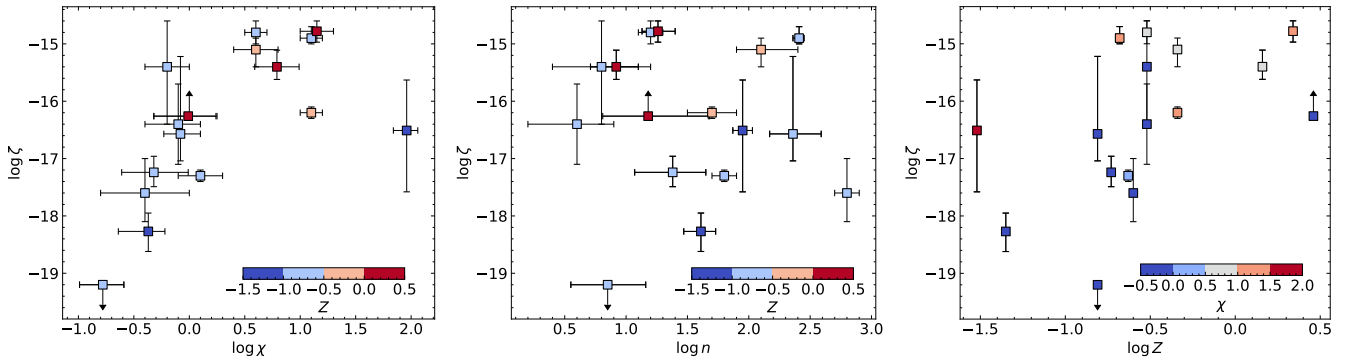


Figure 4. Estimated cosmic-ray ionization rate, ζ , as a function of UV field strength (left panel), number density (middle panel), and metallicity (right panel), using the HD/ H_2 relative abundance measured in DLAs at high redshift. The points are color-coded by metallicity (left and middle panels) and UV field strength (right panel), with color bars provided within each panel.

the range 18 – 20 the dispersion is significantly reduced and only within 1 dex, in comparison with the 3-dex dispersion of ζ in Figure 3 (at the same time, we have not found a significant correlation of $\sqrt{\zeta}/\chi$ with neither Z nor n). As already discussed, the single outlier value of $\sqrt{\zeta}/\chi$ with the highest $\log N(H_2)$ (corresponding to J0843+0221) can be related to cosmic-ray propagation effects at high column densities, or its exceptionally-low metallicity. In turn, at the lower column-density end, absorption systems probe very

diffuse gas, where the application of the H/H_2 and D/HD transition model that we used should be taken with caution. The most important issue, in our opinion, is that the HD/ H_2 ratio primarily depends on the hydrogen ionization fraction of the medium, while the CRIR was derived assuming that this ionization state of the diffuse ISM is mainly determined by CRIR and recombination on dust grains (Balashev & Kosenko 2020). In the case of a very diffuse medium, one can expect that the hydrogen ionization fraction is higher due to

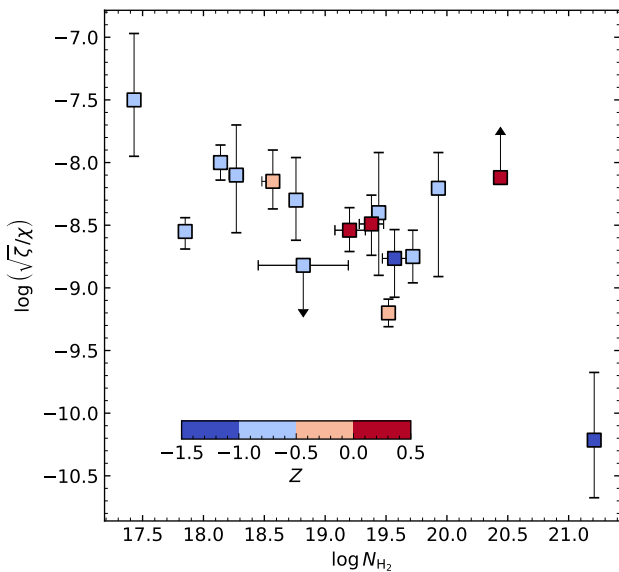


Figure 5. $\sqrt{\zeta}/\chi$ as a function of H_2 column density. The points are color-coded by metallicity using the color bar shown at the bottom.

mixing with ionized and/or warm neutral media, the latter being mostly atomic and hence having higher ionization fractions. All this can effectively mimic the increase of the $\sqrt{\zeta}/\chi$ ratio at lower $\log N(H_2)$ values, that one can notice in Fig. 5. Additionally, the recombination rate coefficient can have a non-linear dependence on the metallicity (in our model, we assume it is linear), since it strongly depends on the properties of the dust and we have no strict constraints on it as a function of the metallicity. Indeed a possible correlation of ζ with Z (see right panel of Fig. 4; excluding J0843+0221 as a possible outlier, we obtain a correlation coefficient of 0.67 with p-value 0.012) can be caused by this non-linear behaviour. Therefore, we caution to use a simple homogeneous model to estimate CRIR at low H_2 column densities. Otherwise, one can propose a physical explanation of the correlation of ζ with Z , as higher metallicity systems probe more massive galaxies (from well-known mass-metallicity relations (see, e.g., Sanders et al. 2015), where star formation on average is expected to be higher than in low-mass galaxies and the cosmic-ray flux (and therefore CRIR) is expected to be enhanced.

7 CONCLUSION

We have presented new measurements of HD molecules in high- z absorption systems found in quasar spectra. We looked for HD in all known strong H_2 -bearing systems and we detected HD molecules in four DLAs and placed upper limits on the HD column density for another twelve DLAs. So with this study, we significantly increased the sample of HD-bearing DLAs. We find that HD/ H_2 relative abundances show large dispersion around the D/H isotopic ratio. This together with previously-known inputs from the modelling of the ISM chemistry indicate that HD/ H_2 ratios cannot be used to constrain the primordial D/H value. In turn, observed HD/ H_2 ratios can be used to estimate the gas phys-

ical conditions, in particular the cosmic-ray ionization rate (CRIR; Balashev & Kosenko 2020). We find that the CRIR varies from a few 10^{-18} s^{-1} to a few 10^{-15} s^{-1} in our sample of high-redshift absorbers, that likely reflects the wide range of environments and physical conditions probed by DLAs. These ranges and dispersion are also in line with previous measurements using various methods in the Galaxy as well as other galaxies.

We find that the CRIR is highly correlated with the UV field intensity in our sample, while it does not correlate with number density and only slightly with metallicity. These correlations suggest a physical connection between the sources of cosmic rays and those of UV radiation. Moreover, we find a quadratic dependence of ζ on χ in our sample, which is probably due to transport effects of low-energy cosmic rays. We caution however that these correlations may be artificial because of the dependence of $N(HD)/N(H_2)$ on combination of ζ , χ , and Z .

Additionally, most of the methods currently used to determine CRIR involve a detailed chemical modeling of the regions related to the diffuse and translucent ISM. Being the dominant species in this region that determine the chemical network results, H_2 can be subject to strong systematics concerning the time-dependent chemistry, since the formation timescale of H_2 can be relatively high in comparison with cloud lifetimes and steady-state models may not be appropriate (e.g., Balashev et al. 2010).

ACKNOWLEDGEMENTS

This work was supported by RSF grant 18-12-00301. We acknowledge support from the French *Centre National de la Recherche Scientifique* through the Russian-French collaborative research program “The diffuse interstellar medium of high redshift galaxies” and from the French *Agence Nationale de la Recherche* under ANR grant 17-CE31-0011-01, project “HIH2” (PI: Noterdaeme).

DATA AVAILABILITY

The results of this paper are based on open data retrieved from the ESO and KECK telescope archives. These data can be shared on reasonable requests to the authors.

REFERENCES

- Albornoz Vázquez D., Rahmani H., Noterdaeme P., Petitjean P., Srianand R., Ledoux C., 2014, *Astron. Astroph.*, **562**, A88
- Asplund M., Grevesse N., Sauval A. J., Scott P., 2009, *Ann. Rev. Astron. Astroph.*, **47**, 481
- Balashev S. A., Kosenko D. N., 2020, *MNRAS*, **492**, L45
- Balashev S. A., Noterdaeme P., 2018, *MNRAS*, **478**, L7
- Balashev S. A., Varshalovich D. A., Ivanchik A. V., 2009, *Astronomy Letters*, **35**, 150
- Balashev S. A., Ivanchik A. V., Varshalovich D. A., 2010, *Astronomy Letters*, **36**, 761
- Balashev S. A., Petitjean P., Ivanchik A. V., Ledoux C., Srianand R., Noterdaeme P., Varshalovich D. A., 2011, *MNRAS*, **418**, 357
- Balashev S. A., Klimenko V. V., Ivanchik A. V., Varshalovich D. A., Petitjean P., Noterdaeme P., 2014, *MNRAS*, **440**, 225

- Balashev S. A., et al., 2017, *MNRAS*, **470**, 2890
- Balashev S. A., et al., 2019, *MNRAS*, **490**, 2668
- Balashev S. A., Ledoux C., Noterdaeme P., Srianand R., Petitjean P., Gupta N., 2020, *MNRAS*, **497**, 1946
- Bergeron J., Boissé P., 2017, *Astron. Astroph.*, **604**, A37
- Carswell R. F., Jorgenson R. A., Wolfe A. M., Murphy M. T., 2011, *MNRAS*, **411**, 2319
- Caselli P., Walmsley C. M., Terzieva R., Herbst E., 1998, *Astroph. J.*, **499**, 234
- Cen R., 2012, *Astroph. J.*, **748**, 121
- Ćirković M. M., Damjanov I., Lalović A., 2006, *Baltic Astronomy*, **15**, 571
- Dekker H., D’Odorico S., Kaufer A., Delabre B., Kotzlowski H., 2000, in Iye M., Moorwood A. F., eds, *Society of Photo-Optical Instrumentation Engineers (SPIE) Conference Series Vol. 4008, Optical and IR Telescope Instrumentation and Detectors*. pp 534–545, doi:10.1117/12.395512
- Draine B. T., 1978, *Astroph. J. Suppl.*, **36**, 595
- Dvorkin I., Vangioni E., Silk J., Petitjean P., Olive K. A., 2016, *MNRAS*, **458**, L104
- Federman S. R., Weber J., Lambert D. L., 1996, *Astroph. J.*, **463**, 181
- Field G. B., Goldsmith D. W., Habing H. J., 1969, *Astroph. J. Lett.*, **155**, L149
- Foreman-Mackey D., Hogg D. W., Lang D., Goodman J., 2013, *Pub. Astron. Soc. Pacific*, **125**, 306
- González-Alfonso E., et al., 2013, *Astron. Astroph.*, **550**, A25
- González-Alfonso E., et al., 2018, *Astroph. J.*, **857**, 66
- Goodman J., Weare J., 2010, *Communications in Applied Mathematics and Computational Science*, **5**, 65
- Guimarães R., Noterdaeme P., Petitjean P., Ledoux C., Srianand R., López S., Rahmani H., 2012, *Astron. J.*, **143**, 147
- Hartquist T. W., Doyle H. T., Dalgarno A., 1978, *Astron. Astroph.*, **68**, 65
- Heiles C., Troland T. H., 2003, *Astroph. J.*, **586**, 1067
- Indriolo N., McCall B. J., 2012, *Astroph. J.*, **745**, 91
- Indriolo N., Geballe T. R., Oka T., McCall B. J., 2007, *Astroph. J.*, **671**, 1736
- Indriolo N., et al., 2015, *Astroph. J.*, **800**, 40
- Indriolo N., Bergin E. A., Falgarone E., Godard B., Zwaan M. A., Neufeld D. A., Wolfire M. G., 2018, *Astroph. J.*, **865**, 127
- Ivanchik A. V., Petitjean P., Balashev S. A., Srianand R., Varshalovich D. A., Ledoux C., Noterdaeme P., 2010, *MNRAS*, **404**, 1583
- Ivanchik A. V., Balashev S. A., Varshalovich D. A., Klimenko V. V., 2015, *Astronomy Reports*, **59**, 100
- Jorgenson R. A., Wolfe A. M., Prochaska J. X., Carswell R. F., 2009, *Astroph. J.*, **704**, 247
- Jorgenson R. A., Wolfe A. M., Prochaska J. X., 2010, *Astroph. J.*, **722**, 460
- Jorgenson R. A., Murphy M. T., Thompson R., Carswell R. F., 2014, *MNRAS*, **443**, 2783
- Kim G., et al., 2020, *Astroph. J. Suppl.*, **249**, 33
- Klimenko V. V., Balashev S. A., 2020, arXiv e-prints, p. arXiv:2007.12231
- Klimenko V. V., Balashev S. A., Ivanchik A. V., Ledoux C., Noterdaeme P., Petitjean P., Srianand R., Varshalovich D. A., 2015, *MNRAS*, **448**, 280
- Klimenko V. V., Balashev S. A., Ivanchik A. V., Varshalovich D. A., 2016, *Astronomy Letters*, **42**, 137
- Kosenko D. N., Balashev S. A., 2018, *J.Phys.: Conf. Series*, **1135**, 012009
- Lacour S., Ziskin V., Hébrard G., Oliveira C., André M. K., Ferlet R., Vidal-Madjar A., 2005, *Astroph. J.*, **627**, 251
- Le Petit F., Roueff E., Le Bourlot J., 2002, *Astron. Astroph.*, **390**, 369
- Le Petit F., Ruaud M., Bron E., Godard B., Roueff E., Languignon D., Le Bourlot J., 2016, *Astron. Astroph.*, **585**, A105
- Ledoux C., Petitjean P., Srianand R., 2003, *MNRAS*, **346**, 209
- Ledoux C., Noterdaeme P., Petitjean P., Srianand R., 2015, *Astron. Astroph.*, **580**, A8
- Liszt H. S., 2015, *Astroph. J.*, **799**, 66
- Maret S., Bergin E. A., 2007, *Astroph. J.*, **664**, 956
- McKee C. F., Ostriker J. P., 1977, *Astroph. J.*, **218**, 148
- Muller S., et al., 2016, *Astron. Astroph.*, **595**, A128
- Murphy M. T., Kacprzak G. G., Savorgnan G. A. D., Carswell R. F., 2019, *MNRAS*, **482**, 3458
- Neeleman M., Prochaska J. X., Wolfe A. M., 2015, *Astroph. J.*, **800**, 7
- Neufeld D. A., Wolfire M. G., 2017, *Astroph. J.*, **845**, 163
- Noterdaeme P., Ledoux C., Petitjean P., Le Petit F., Srianand R., Smette A., 2007, *Astron. Astroph.*, **474**, 393
- Noterdaeme P., Petitjean P., Ledoux C., Srianand R., Ivanchik A., 2008, *Astron. Astroph.*, **491**, 397
- Noterdaeme P., Petitjean P., Ledoux C., López S., Srianand R., Vergani S. D., 2010, *Astron. Astroph.*, **523**, A80
- Noterdaeme P., Petitjean P., Pâris I., Cai Z., Finley H., Ge J., Pieri M. M., York D. G., 2014, *Astron. Astroph.*, **566**, A24
- Noterdaeme P., Srianand R., Rahmani H., Petitjean P., Pâris I., Ledoux C., Gupta N., López S., 2015, *Astron. Astroph.*, **577**, A24
- Noterdaeme P., et al., 2017, *Astron. Astroph.*, **597**, A82
- Noterdaeme P., Ledoux C., Zou S., Petitjean P., Srianand R., Balashev S., López S., 2018, *Astron. Astroph.*, **612**, A58
- O’Meara J. M., Lehner N., Howk J. C., Prochaska J. X., Fox A. J., Peebles M. S., Tumlinson J., O’Shea B. W., 2017, *Astron. J.*, **154**, 114
- Oliveira C. M., Sembach K. R., Tumlinson J., O’Meara J., Thom C., 2014, *Astroph. J.*, **783**, 22
- Padovani M., Galli D., Glassgold A. E., 2009, *Astron. Astroph.*, **501**, 619
- Padovani M., Ivlev A. V., Galli D., Caselli P., 2018, *Astron. Astroph.*, **614**, A111
- Padovani M., et al., 2020, *Space Sci. Rev.*, **216**, 29
- Pitrou C., Coc A., Uzan J.-P., Vangioni E., 2018, *Phys. Rep.*, **754**, 1
- Planck Collaboration et al., 2020, *Astron. Astroph.*, **641**, A6
- Prochaska J. X., Howk J. C., Wolfe A. M., 2003, *Nature*, **423**, 57
- Rahmani H., et al., 2013, *MNRAS*, **435**, 861
- Ranjan A., et al., 2018, *Astron. Astroph.*, **618**, A184
- Ranjan A., Noterdaeme P., Krogager J. K., Petitjean P., Srianand R., Balashev S. A., Gupta N., Ledoux C., 2020, *Astron. Astroph.*, **633**, A125
- Rawlins K., Srianand R., Shaw G., Rahmani H., Dutta R., Chacko S., 2018, *MNRAS*, **481**, 2083
- Sanders R. L., et al., 2015, *Astroph. J.*, **799**, 138
- Shaw G., Ferland G. J., Srianand R., Abel N. P., van Hoof P. A. M., Stancil P. C., 2008, *Astroph. J.*, **675**, 405
- Shaw G., Rawlins K., Srianand R., 2016, *MNRAS*, **459**, 3234
- Silbsbee K., Ivlev A. V., 2019, *Astroph. J.*, **879**, 14
- Snow T. P., Ross T. L., Destree J. D., Drosback M. M., Jensen A. G., Rachford B. L., Sonnentrucker P., Ferlet R., 2008, *Astroph. J.*, **688**, 1124
- Snowden S. L., et al., 1997, *Astroph. J.*, **485**, 125
- Srianand R., Petitjean P., Ledoux C., Ferland G., Shaw G., 2005, *MNRAS*, **362**, 549
- Srianand R., Noterdaeme P., Ledoux C., Petitjean P., 2008, *Astron. Astroph.*, **482**, L39
- Tumlinson J., et al., 2010, *Astroph. J.*, **718**, L156
- Varshalovich D. A., Ivanchik A. V., Petitjean P., Srianand R., Ledoux C., 2001, *Astronomy Letters*, **27**, 683
- Vernet J., et al., 2011, *Astron. Astroph.*, **536**, A105
- Vogt S. S., et al., 1994, in Crawford D. L., Craine E. R., eds, *Society of Photo-Optical Instrumentation Engineers (SPIE) Conference Series Vol. 2198, Instrumentation in Astronomy VIII*. p. 362, doi:10.1117/12.176725

- Wolfe A. M., Gawiser E., Prochaska J. X., 2005, [Ann. Rev. Astron. Astroph.](#), **43**, 861
- Zou S., Petitjean P., Noterdaeme P., Ledoux C., Krogager J. K., Fathivavsari H., Srianand R., López S., 2018, [Astron. Astroph.](#), **616**, A158
- van Dishoeck E. F., Black J. H., 1986, [Astroph. J. Suppl.](#), **62**, 109
- van der Tak F. F. S., Weiß A., Liu L., Güsten R., 2016, [Astron. Astroph.](#), **593**, A43

APPENDIX A: PROFILE FITTING RESULTS

A1 HD line profiles

Figures [A1-A16](#) show the line profiles of HD lines in the DLAs studied in this paper and listed in Table [3](#).

A2 Fit results of absorption lines towards J 0917+0154

In Table [A1](#) we present results of the fitting of C I, H₂ and HD lines in the DLA at $z = 2.106$ towards J 0917+0154 using 3-component model. Figure [A17](#) shows the profiles of H₂ absorption lines, while in Figure [A4](#) we present the fit to C I and HD lines.

A3 DLA at J 0812+3208

In this section we present results of the fitting of H₂ and HD lines in the DLA at $z = 2.067$ towards J 0812+3208. Table [A2](#) provides detailed result of the fitting and Figure [A18](#) shows line profiles of H₂ and HD absorption lines.

A4 Fit results of H₂/HD towards J 0816+1446

In this section we present results of HD₂ and HD fitting in the DLA at $z = 3.287$ using 3-component model. Table [A3](#) provides HD and H₂ fit results and HD line profiles are shown in Figure [A13](#).

A5 Fit results of H₂/CI towards J 1311+2225

In this section we present detailed results of the fitting of H₂ and C I in the DLA at $z=3.09$ towards J 1311+2225 using 4-component model. Table [A4](#) provided the fitted values, while Figures [A19](#) and [A20-A23](#) show line profiles of C I and H₂ absorption lines, respectively.

A6 Fit results of H₂/CI towards J 2340–0053

In this section we present detailed results of the fitting of H₂ and C I in the DLA at $z=2.05$ towards J 2340–0053 using 7-component model. Table [A5](#) provided the fitted values, while Figures [A25](#) and [A26-A28](#) show C I and H₂ absorption lines, respectively.

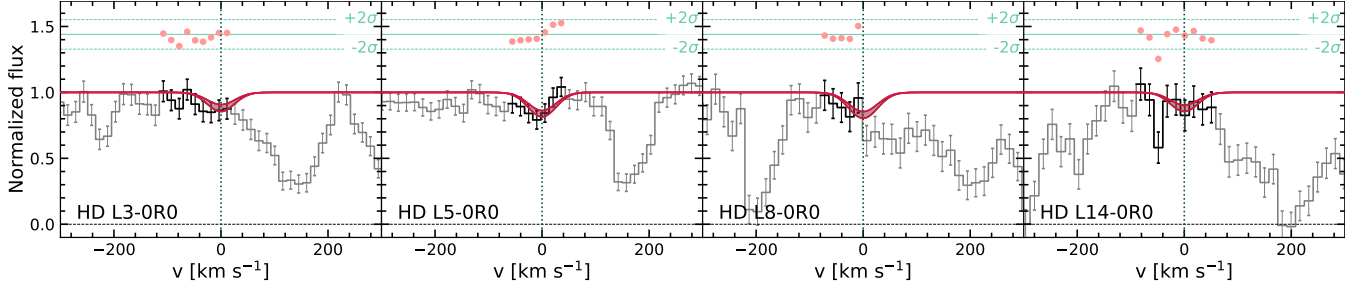


Figure A1. Fit to HD absorption lines in DLA at $z=2.77943$ in J0136+0440. The gray and black lines show whole spectra and only pixels used to derive column density, respectively. The red lines indicate the fit profile to HD absorption lines. The region between lines enclose to 0.68 central percentile interval for the fit models, which are sampled from the obtained posterior probability distribution of the parameters. The red points at the top of each panel show the residuals, for the median profile. The vertical dashed lines indicate the central position of the velocity components.

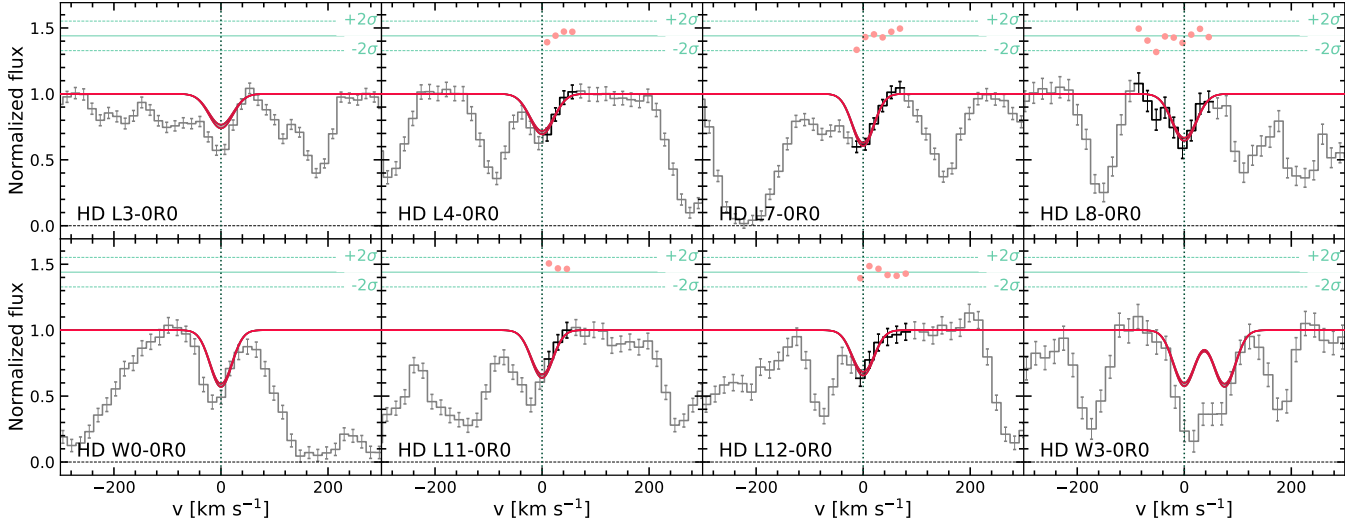


Figure A2. Fit to HD absorption lines in DLA at $z=2.62524$ in J0858+1749. The lines are the same as in Fig. A1.

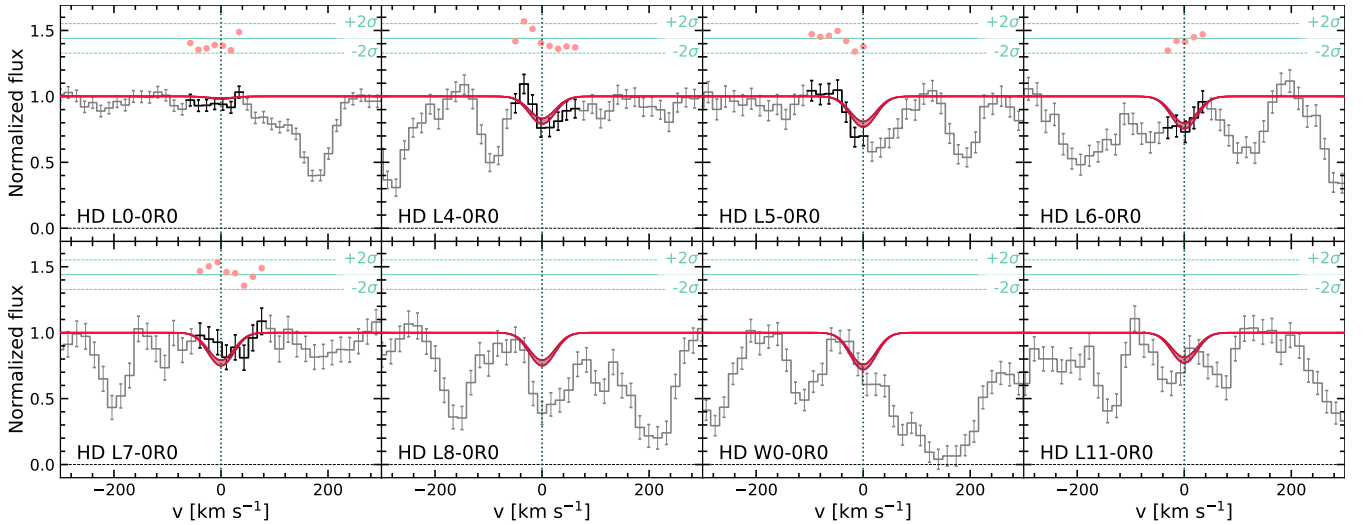


Figure A3. Fit to HD absorption lines in DLA at $z=2.56918$ in J0906+0548. The lines are the same as in Fig. A1.

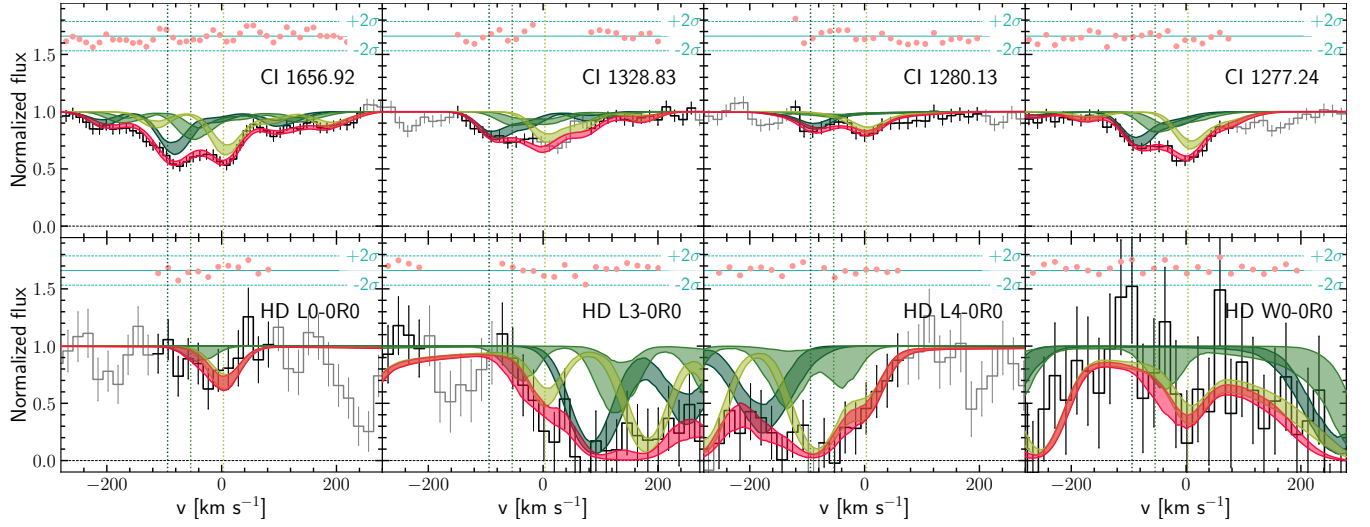


Figure A4. Fit to CI and HD absorption lines in DLA in J0917-0154. The lines are the same as in Fig. A1. The green lines and regions correspond to the contribution of each velocity component. In that particular system all HD lines, except L0-0R(0), are significantly blended with H₂ absorption lines, for which the fit is shown in Fig. A17.

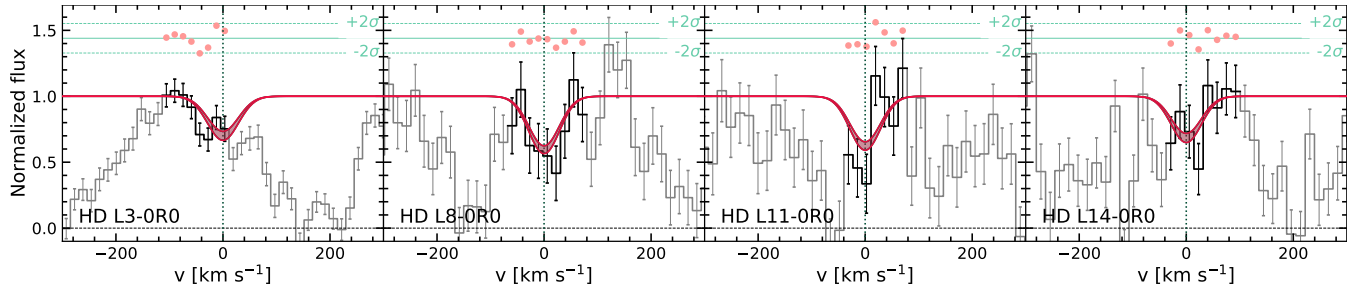


Figure A5. Fit to HD absorption lines in DLA at $z=2.606406$ in J0946+1216. The lines are the same as in Fig. A1.

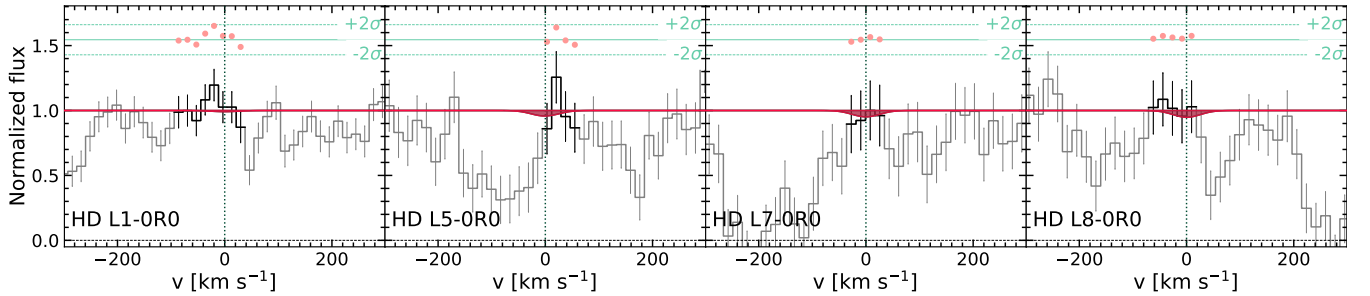


Figure A6. Fit to HD absorption lines in DLA at $z=2.3228054$ in J1143+1420. The lines are the same as in Fig. A1.

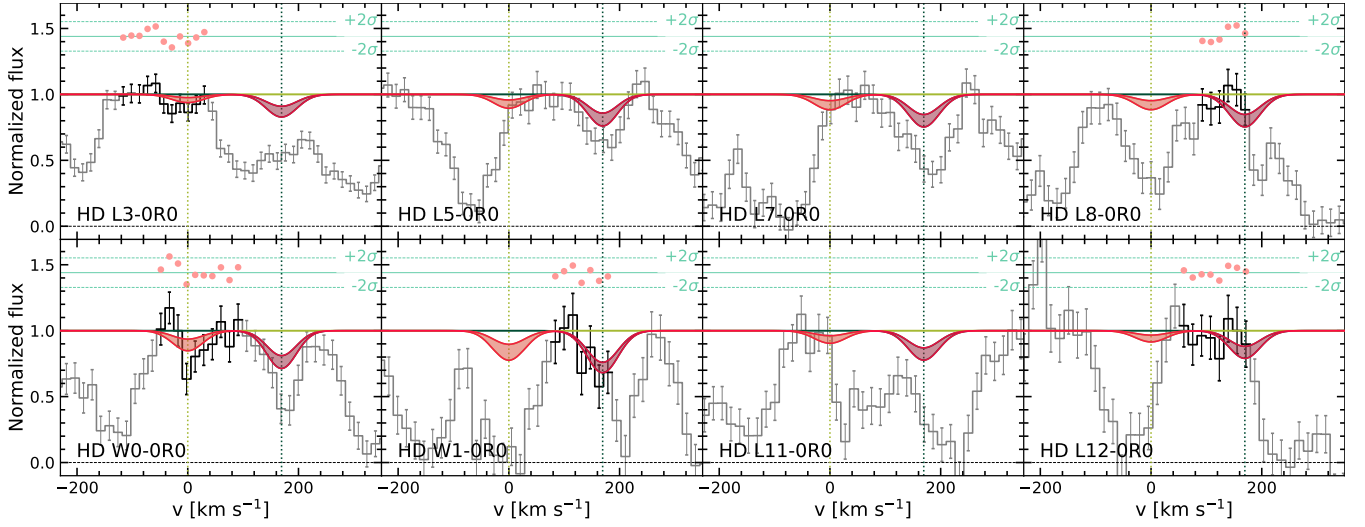


Figure A7. Spectrum of J1146+0743 at the position of expected HD absorption lines from DLA at $z \approx 2.840$. The lines are the same as in Fig. A4, except the red lines show the profiles of HD lines with column densities correspond to the upper limits reported in Table 3.

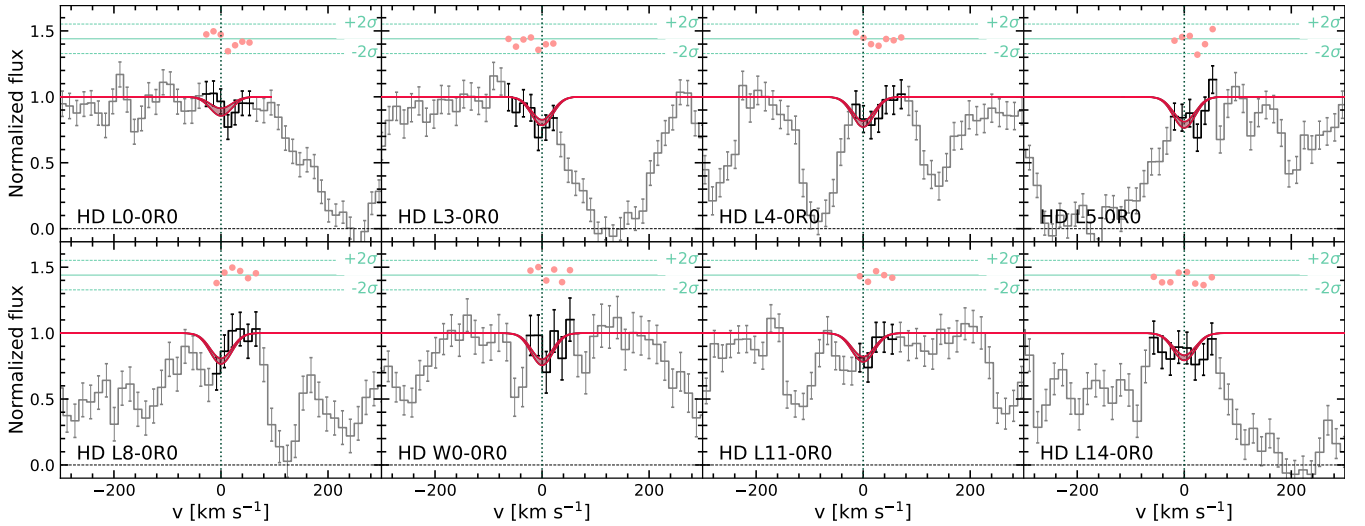


Figure A8. Fit to HD absorption lines in DLA at $z=3.03292$ in J1236+0010. The lines are the same as in Fig. A1.

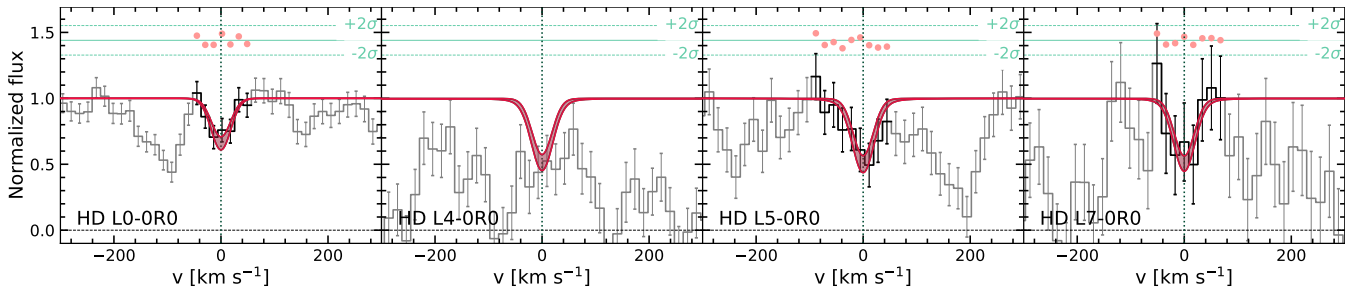


Figure A9. Fit to HD absorption lines in DLA at $z=2.58796$ in J1513+0352. The lines are the same as in Fig. A1.

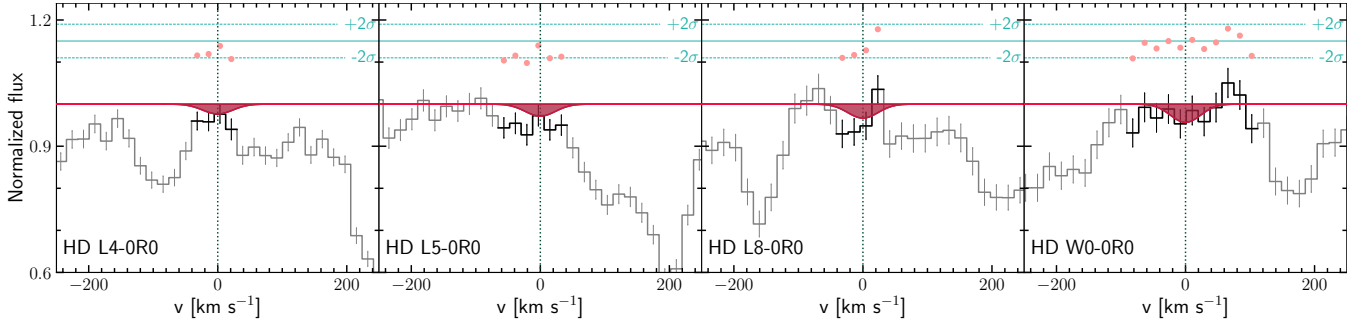


Figure A10. Fit to HD absorption lines in DLA at $z=2.279378$ in J2232+1242. The lines are the same as in Fig. A1.

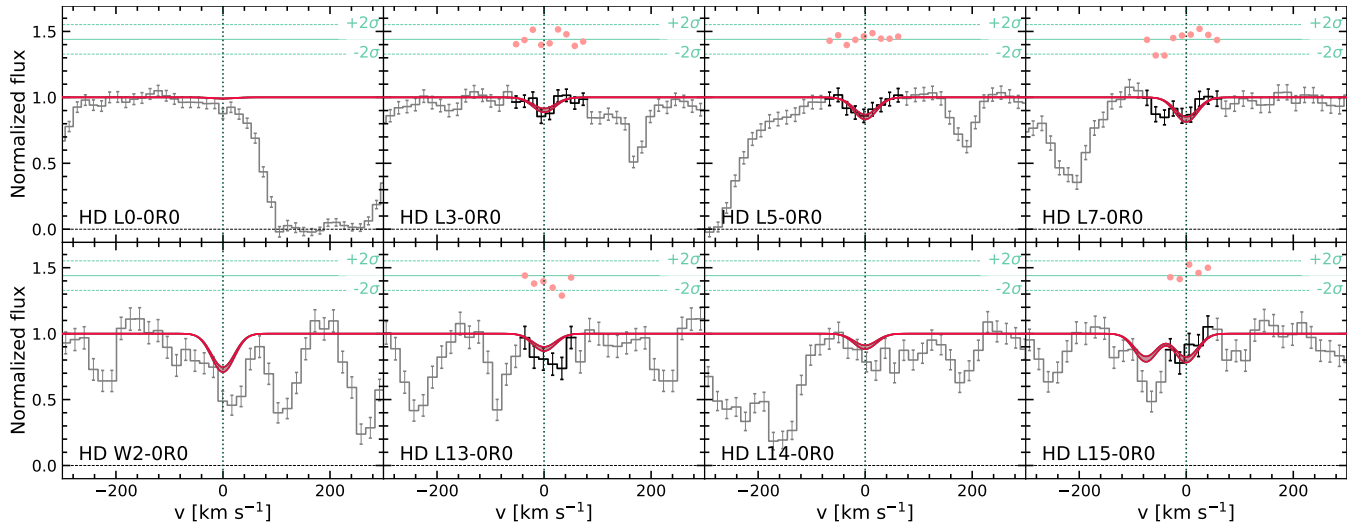


Figure A11. Fit to HD absorption lines in DLA at $z=2.58797$ in J2347+0051. The lines are the same as in Fig. A1.

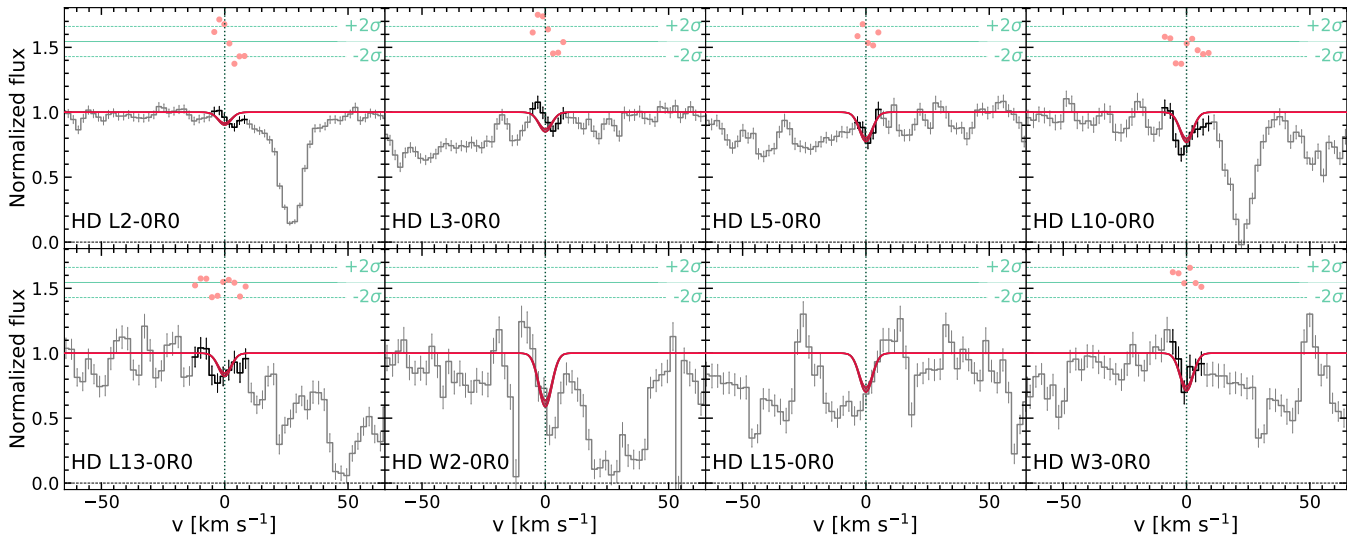


Figure A12. Fit to HD absorption lines in DLA towards HE0027+1836. The lines are the same as in Fig. A1.

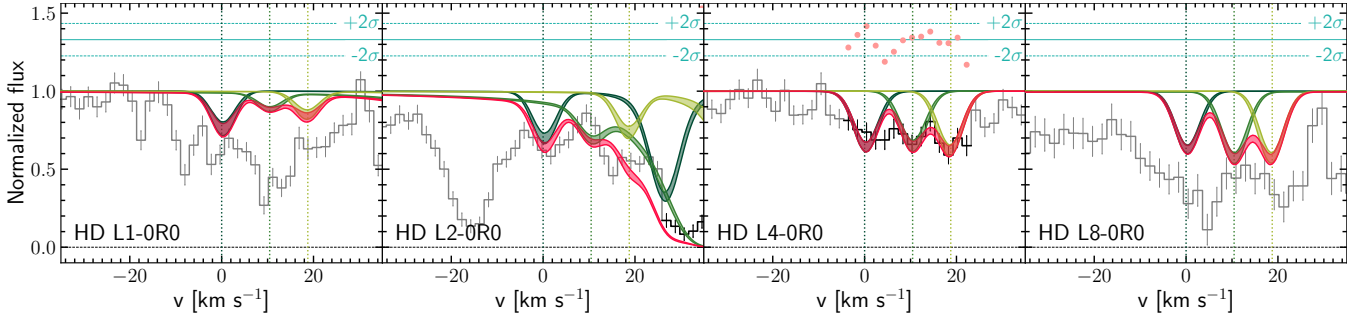


Figure A13. Fit to HD absorption lines in DLA towards J0816+1446. The lines are the same as in Fig. A4.

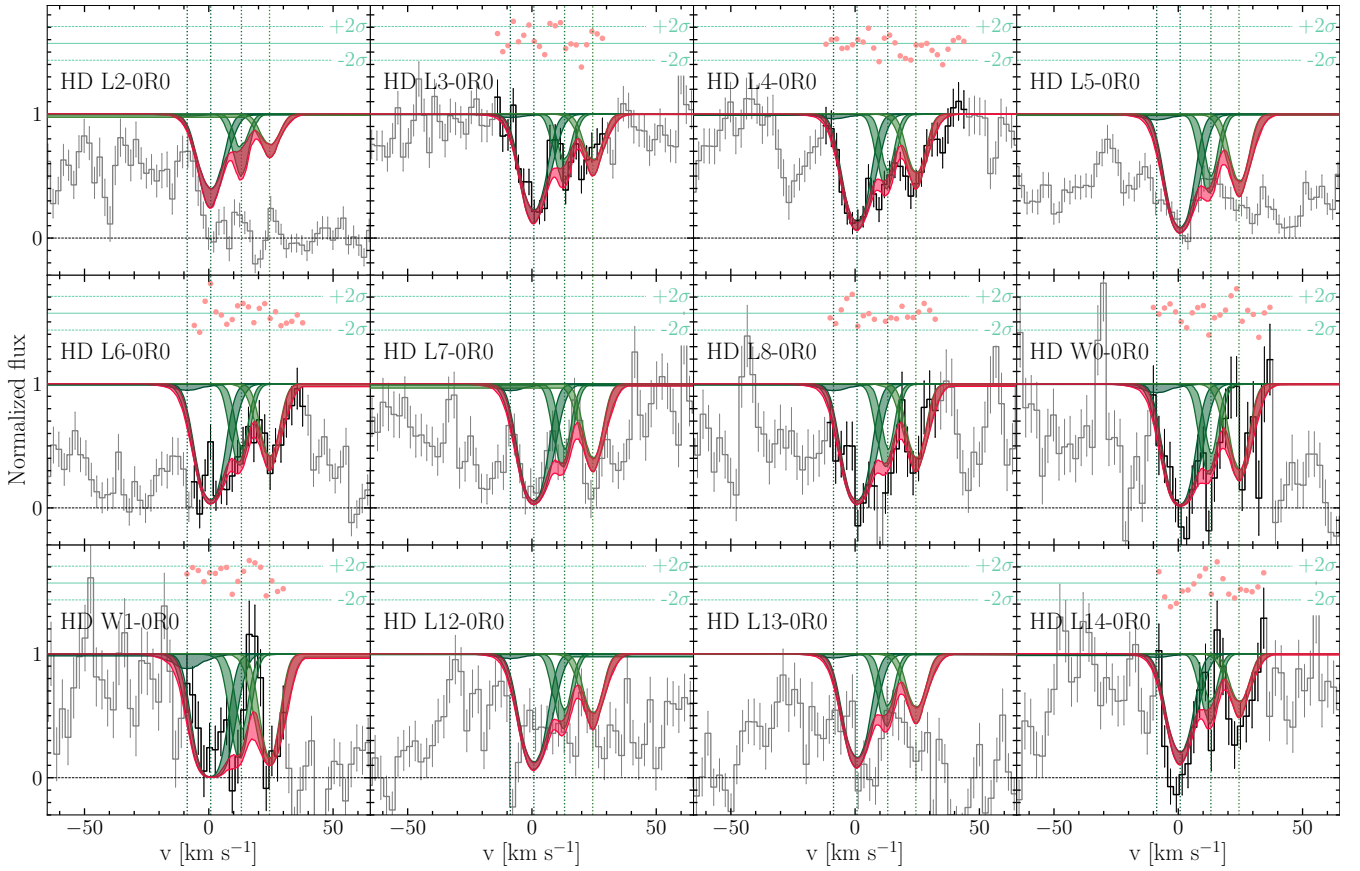


Figure A14. Fit to HD absorption lines in DLA towards J1311+2225. The lines are the same as in Fig. A4.

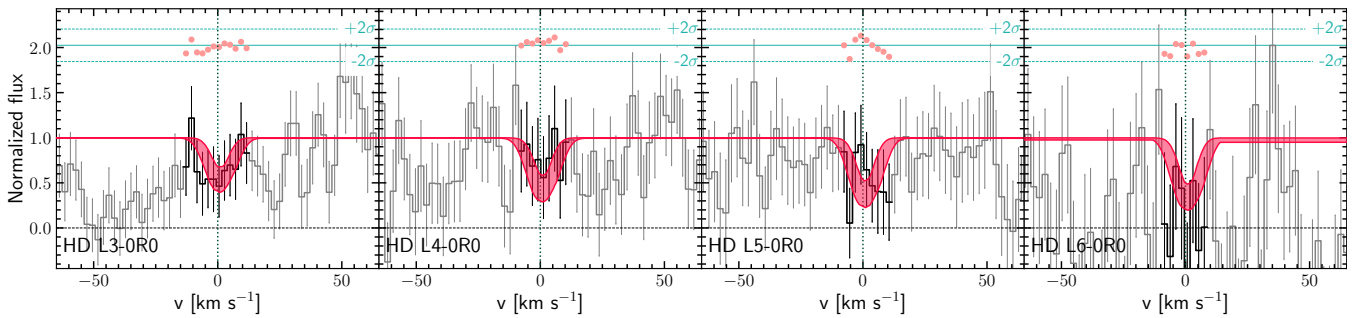


Figure A15. Fit to HD absorption lines in DLA towards J2140-1840. The lines are the same as in Fig. A1.

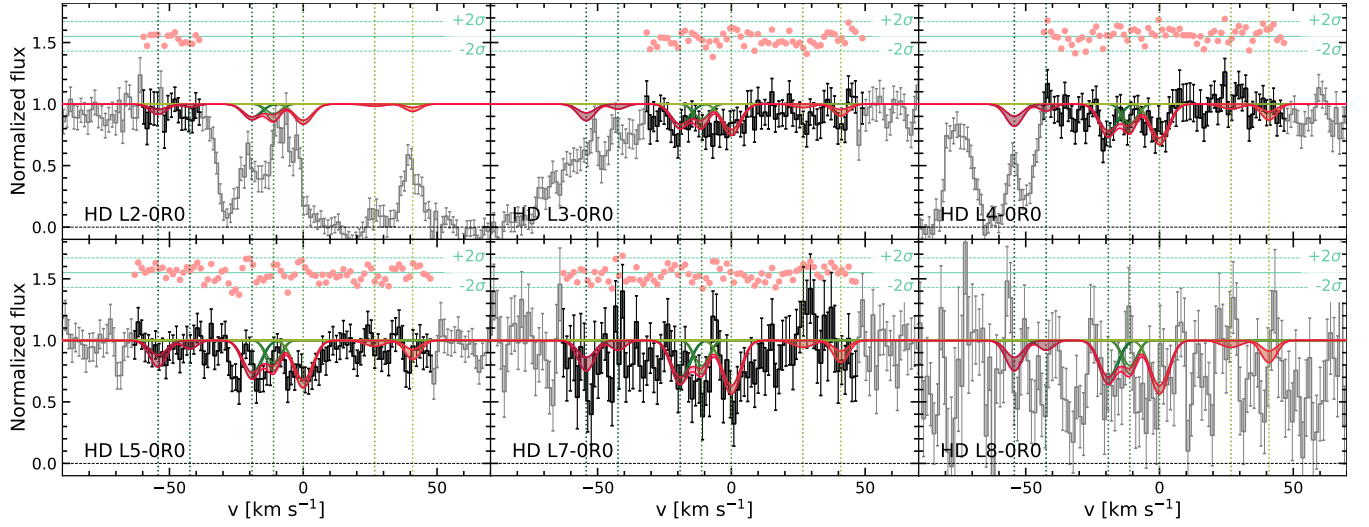


Figure A16. Fit to HD absorption lines in DLA at $z = 2.055$ in J 2340–0053. The lines are the same as in Fig. A4.

Table A1. Fit results of C I, H₂, and HD lines $z = 2.106$ towards J 0917–0154.

| species | comp | 1 | 2 | 3 | $\log N_{\text{tot}}$ |
|------------------------|-----------------------|-------------------------|--------------------------|----------------------------|-------------------------|
| | z | $2.10586^{(+6)}_{(-3)}$ | $2.10624^{(+13)}_{(-7)}$ | $2.106812^{(+49)}_{(-11)}$ | |
| | Δv , km/s | -95.8 | -46.7 | 0.0 | |
| | b , km/s | $5.2^{+1.1}_{-1.8}$ | $6.4^{+1.5}_{-2.4}$ | $4.7^{+1.1}_{-1.3}$ | |
| CI | $\log N$ | $14.15^{+0.16}_{-0.18}$ | $13.46^{+0.12}_{-0.26}$ | $14.35^{+0.20}_{-0.18}$ | $14.59^{+0.18}_{-0.10}$ |
| CI* | $\log N$ | $13.55^{+0.12}_{-0.20}$ | $13.41^{+0.12}_{-0.19}$ | $13.66^{+0.12}_{-0.15}$ | $13.99^{+0.06}_{-0.08}$ |
| CI** | $\log N$ | $13.30^{+0.17}_{-0.28}$ | $13.02^{+0.21}_{-0.42}$ | $13.29^{+0.18}_{-0.29}$ | $13.67^{+0.09}_{-0.18}$ |
| H ₂ $J = 0$ | $\log N$ | $18.11^{+0.30}_{-0.83}$ | $18.48^{+0.67}_{-0.96}$ | $19.73^{+0.14}_{-0.13}$ | $19.80^{+0.07}_{-0.16}$ |
| H ₂ $J = 1$ | $\log N$ | $17.77^{+0.78}_{-0.35}$ | $17.98^{+1.13}_{-1.13}$ | $19.81^{+0.09}_{-0.07}$ | $19.87^{+0.05}_{-0.09}$ |
| H ₂ $J = 2$ | $\log N$ | $16.30^{+0.26}_{-0.22}$ | $15.95^{+0.69}_{-1.09}$ | $18.14^{+0.26}_{-0.64}$ | $18.18^{+0.13}_{-0.73}$ |
| | b , km/s | $26.9^{+5.5}_{-7.2}$ | $9.2^{+9.6}_{-2.0}$ | $12.1^{+5.3}_{-1.5}$ | |
| H ₂ $J = 3$ | $\log N$ | $15.53^{+0.16}_{-0.16}$ | $14.86^{+0.66}_{-0.70}$ | $16.43^{+0.24}_{-0.17}$ | $16.46^{+0.24}_{-0.12}$ |
| | b , km/s | $29.5^{+9.9}_{-9.6}$ | $15.3^{+0.4}_{-0.5}$ | $21.7^{+3.4}_{-9.1}$ | |
| | $\log N_{\text{tot}}$ | $17.96^{+0.82}_{-0.16}$ | $18.4^{+1.0}_{-0.3}$ | $20.09^{+0.07}_{-0.08}$ | |
| HD $J = 0$ | $\log N$ | < 12 | < 15.9 | < 18.1 | < 18.1 |

The Doppler parameters of C I fine-structure levels, H₂ $J=0,1$ rotational levels, and HD were tied together, while H₂ $J=2,3$ were varied independently, but taking into account penalty function for the Doppler parameters as described in Sect. 3.2.

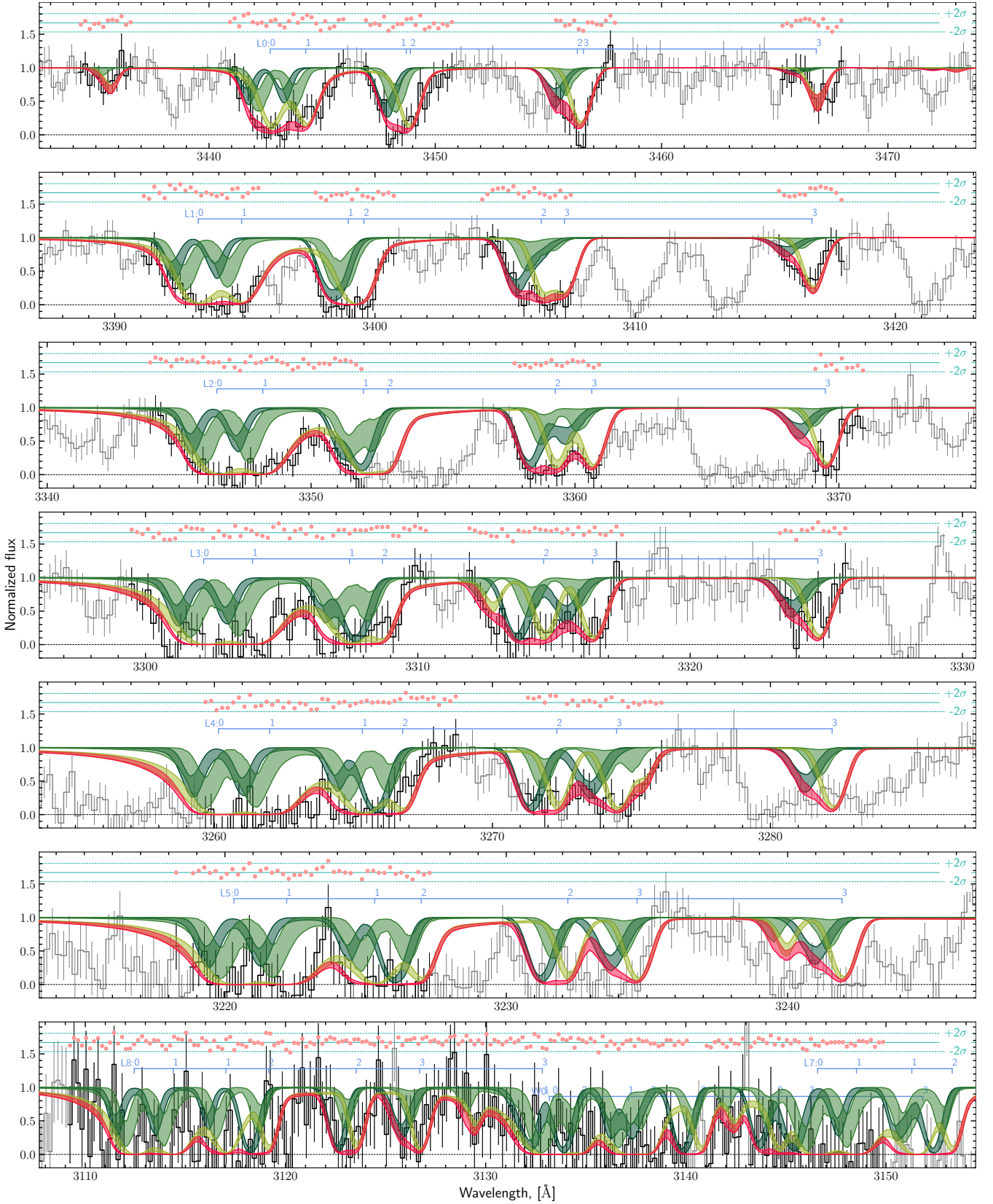


Figure A17. Fit to H₂ and HD absorption lines in DLA at $z = 2.106$ towards J091721.37+015448.1. The lines are the same as in Fig. A4. The blue ticks marks a position of H₂ lines.

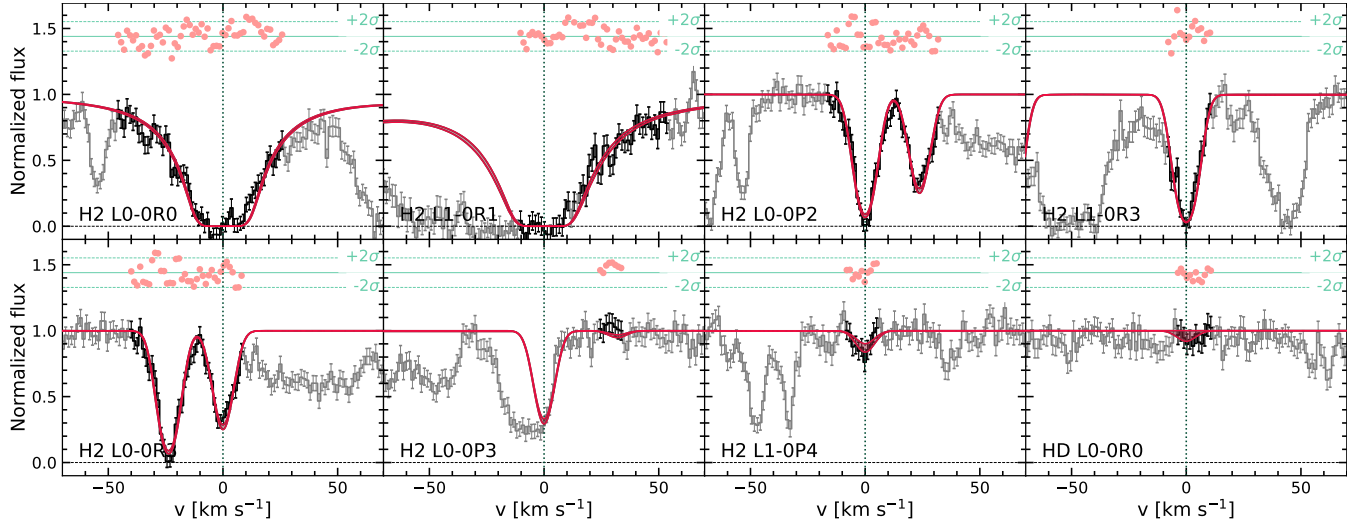


Figure A18. Fit to H₂ and HD absorption lines in DLA at $z=2.06678$ in J0812+0032. The lines are the same as in Fig. A1.

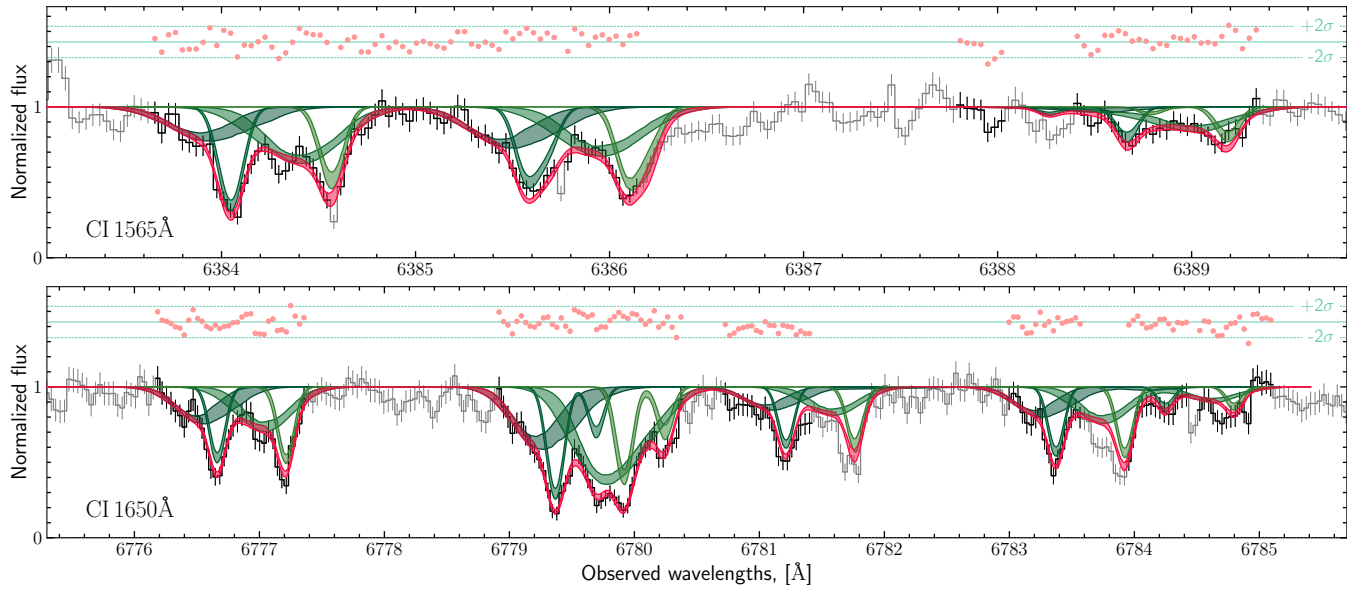


Figure A19. Fit to C I absorption lines in DLA towards J1311+2225. The lines are the same as in Fig. A4.

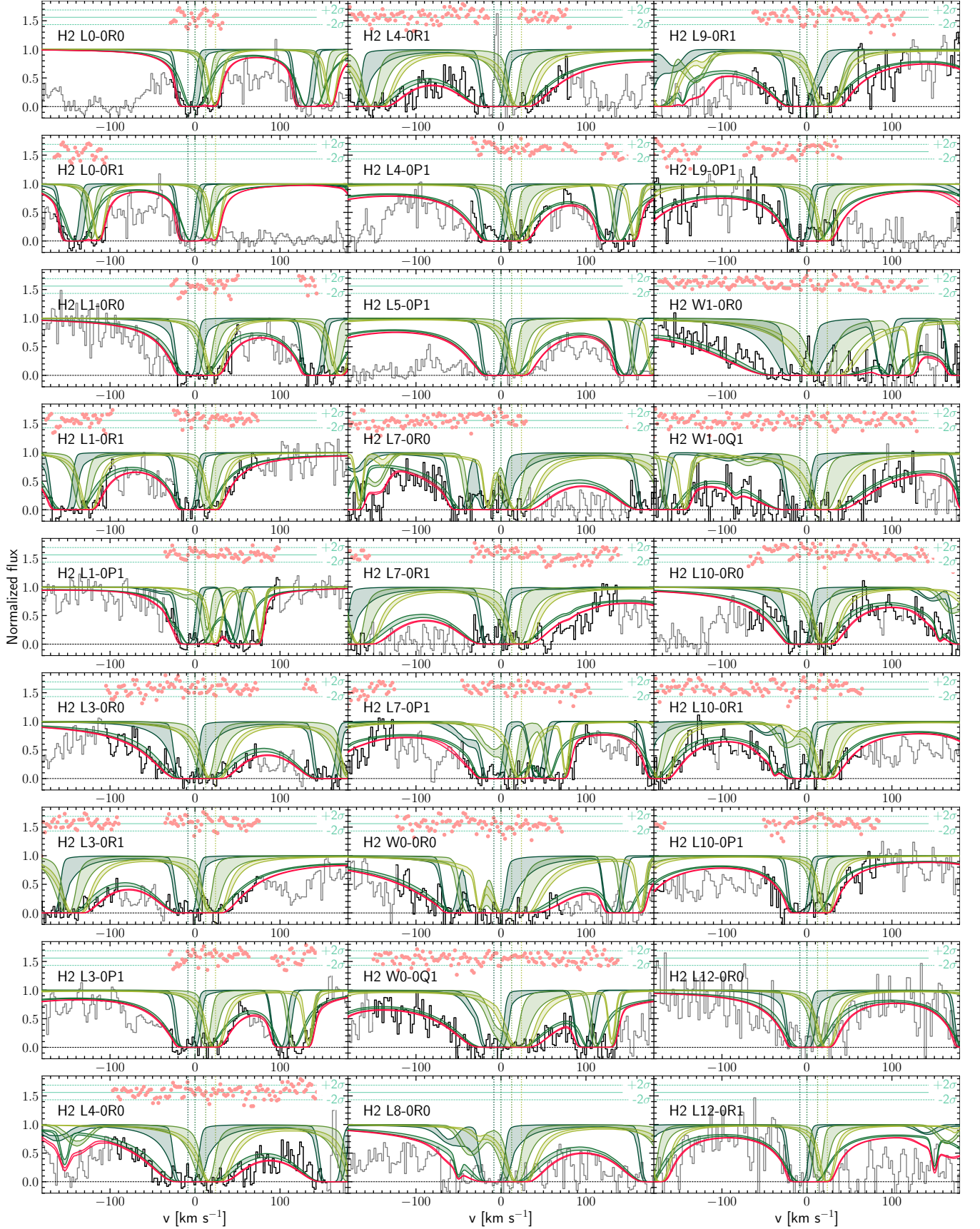


Figure A20. Fit to $J=0, J=1$ H_2 absorption lines in DLA towards J1311+2225. The lines are the same as in Fig. A4.

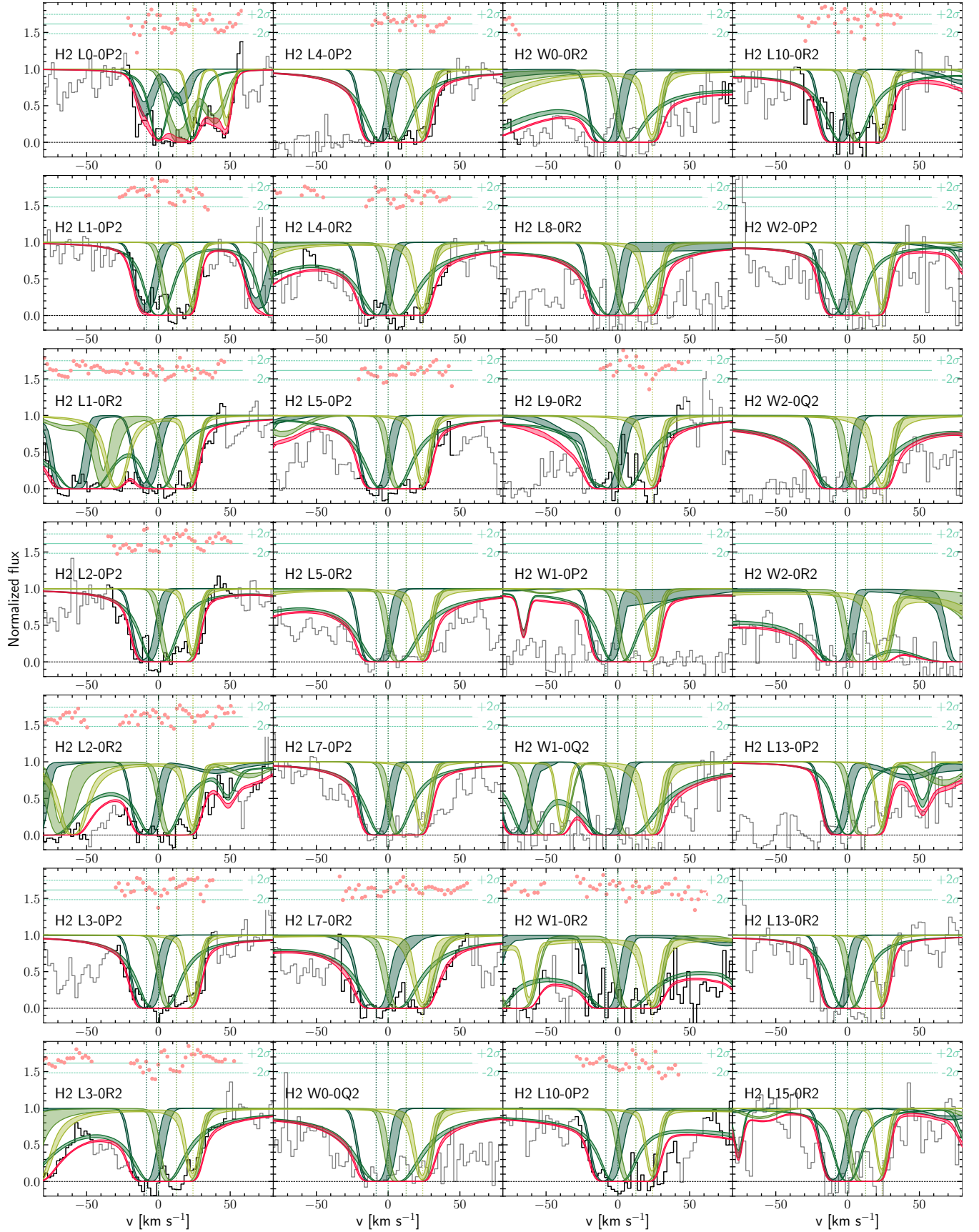


Figure A21. Fit to J=2 H₂ absorption lines in DLA towards J 1311+2225. The lines are the same as in Fig. A4.

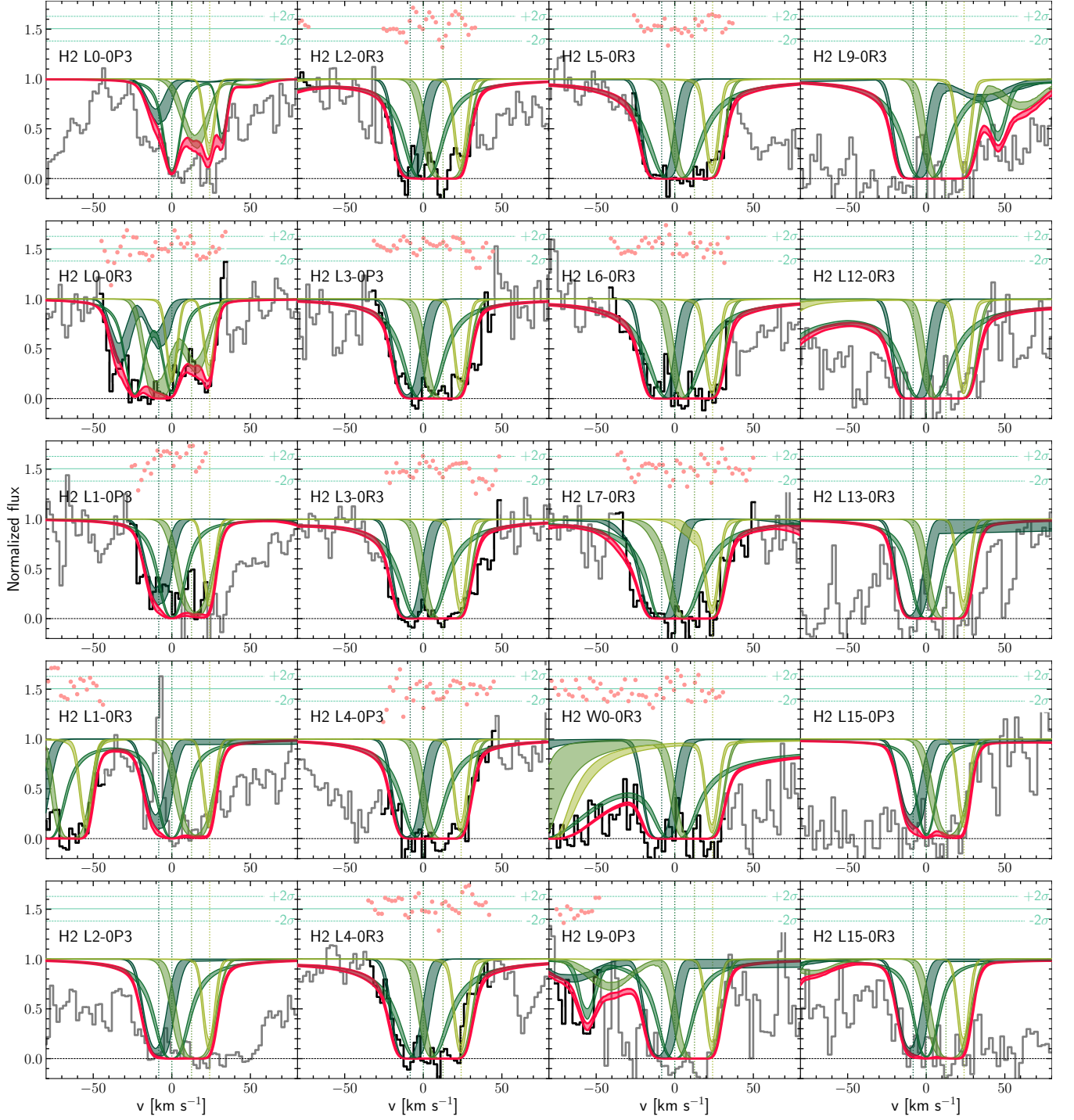


Figure A22. Fit to J=3 H₂ absorption lines in DLA towards J1311+2225. The lines are the same as in Fig. A4.

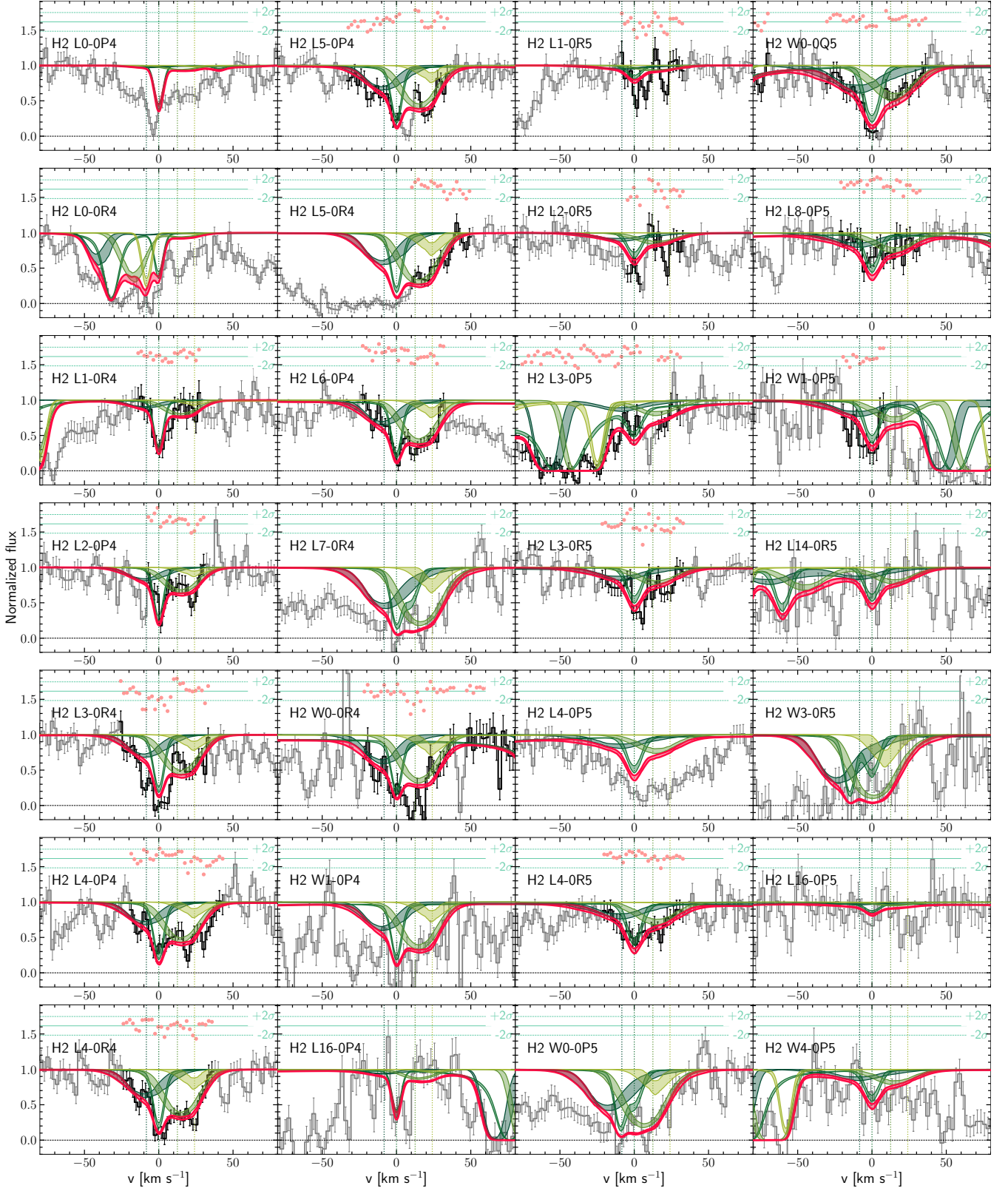


Figure A23. Fit to J=4 and J=5 H₂ absorption lines in DLA towards J1311+2225. The lines are the same as in Fig. A4.

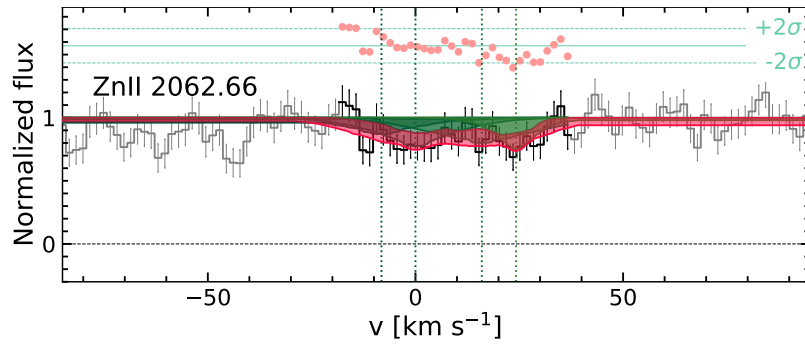


Figure A24. Fit to Zn II absorption lines in DLA towards J1311+2225. The lines are the same as in Fig. A4.

Table A2. Results from H₂ and HD analysis at $z = 2.066780(1)$ towards J 0812+3208.

| | J | b | $\log N$ |
|--------------------|-------|---------------------|-------------------------|
| H ₂ | 0 | $4.4^{+0.1}_{-0.1}$ | $19.03^{+0.02}_{-0.02}$ |
| | 1 | " - | $18.88^{+0.03}_{-0.03}$ |
| | 2 | " - | $16.19^{+0.04}_{-0.03}$ |
| | 3 | " - | $15.76^{+0.03}_{-0.02}$ |
| | 4 | " - | $14.28^{+0.12}_{-0.12}$ |
| | total | | $19.26^{+0.02}_{-0.01}$ |
| HD | 0 | " - | < 14.43 |
| HD/2H ₂ | | | $< 7.39 \times 10^{-6}$ |

Table A3. Fit results of H₂, and HD lines $z = 3.287$ towards J0816+1446.

| species | comp | 1 | 2 | 3 | log N_{tot} |
|--------------------|----------------------|--------------------------|--------------------------|--------------------------|--------------------------|
| | z | 3.287252($^{+3}_{-2}$) | 3.287399($^{+2}_{-3}$) | 3.287515($^{+2}_{-3}$) | |
| | Δv , km/s | -10.0 | 0 | 8.1 | |
| | b , km/s | 0.62 $^{+0.03}_{-0.04}$ | 1.49 $^{+0.05}_{-0.09}$ | 1.07 $^{+0.11}_{-0.12}$ | |
| H ₂ J=0 | log N | 16.25 $^{+0.10}_{-0.12}$ | 17.61 $^{+0.06}_{-0.03}$ | 17.13 $^{+0.09}_{-0.06}$ | 17.76 $^{+0.03}_{-0.02}$ |
| H ₂ J=1 | log N | 16.83 $^{+0.09}_{-0.11}$ | 18.30 $^{+0.03}_{-0.03}$ | 17.39 $^{+0.09}_{-0.15}$ | 18.36 $^{+0.02}_{-0.02}$ |
| H ₂ J=2 | log N | 15.88 $^{+0.12}_{-0.10}$ | 17.43 $^{+0.05}_{-0.06}$ | 16.42 $^{+0.13}_{-0.17}$ | 17.47 $^{+0.04}_{-0.04}$ |
| | b , km/s | 0.76 $^{+0.06}_{-0.05}$ | 1.86 $^{+0.06}_{-0.07}$ | 1.27 $^{+0.07}_{-0.06}$ | |
| H ₂ J=3 | log N | 14.91 $^{+0.09}_{-0.11}$ | 15.55 $^{+0.03}_{-0.02}$ | 15.81 $^{+0.20}_{-0.20}$ | 16.00 $^{+0.15}_{-0.08}$ |
| | b , km/s | 0.77 $^{+0.06}_{-0.08}$ | 3.42 $^{+0.13}_{-0.17}$ | 1.24 $^{+0.07}_{-0.08}$ | |
| | log N_{tot} | 16.97 $^{+0.09}_{-0.10}$ | 18.43 $^{+0.04}_{-0.03}$ | 17.60 $^{+0.10}_{-0.10}$ | |
| HD | log N | < 14.9 | < 14 | < 14.2 | < 15.0 |

The Doppler parameters of H₂ J=0,1 rotational levels, and HD were tied together, while H₂ J=2,3 were varied independently, but taking into account penalty function for the Doppler parameters as described in Sect. 3.2.

Table A4. Fit results of C I, H₂, and HD in DLA at $z = 3.09$ towards J 131129.11+222552.6.

| comp | | 1 | 2 | 3 | 4 | log N_{tot} | |
|------------------------|----------------------|-------------------------------|---|--|---|--|--------------------------|
| z | | 3.091410($^{+21}_{-14}$) | 3.0915350($^{+23}_{-21}$) | 3.091735($^{+12}_{-10}$) | 3.0918577($^{+25}_{-25}$) | | |
| Δv , km/s | | -10.0 | 0.0 | 14.5 | 23.7 | | |
| C I | b , km/s | 11 $^{+1}_{-3}$ | 1.2 $^{+0.4}_{-0.2}$ | 12 $^{+1}_{-2}$ | 1.1 $^{+0.7}_{-0.1}$ | | |
| | log N | 13.17 $^{+0.11}_{-0.11}$ | 13.81 $^{+0.73}_{-0.27}$ | 13.48 $^{+0.05}_{-0.05}$ | 13.32 $^{+0.31}_{-0.20}$ | 14.42 $^{+0.51}_{-0.13}$ | |
| | C I* | log N | 13.28 $^{+0.10}_{-0.11}$ | 13.45 $^{+0.11}_{-0.08}$ | 13.42 $^{+0.07}_{-0.08}$ | 13.40 $^{+0.16}_{-0.09}$ | 13.99 $^{+0.08}_{-0.04}$ |
| | C I** | log N | 12.00 $^{+0.5}_{-0.4}$ | 12.86 $^{+0.07}_{-0.09}$ | 13.14 $^{+0.04}_{-0.11}$ | 12.81 $^{+0.10}_{-0.21}$ | 13.43 $^{+0.04}_{-0.02}$ |
| | log N_{tot} | 13.56 $^{+0.10}_{-0.12}$ | 13.95 $^{+0.61}_{-0.16}$ | 13.85 $^{+0.04}_{-0.06}$ | 13.71 $^{+0.21}_{-0.11}$ | 14.42 $^{+0.34}_{-0.10}$ | |
| H ₂ $J = 0$ | log N | 17.57 $^{+0.56}_{-0.33}$ | 19.07 $^{+0.03}_{-0.05}$ | 17.70 $^{+0.40}_{-0.30}$ | 18.21 $^{+0.08}_{-0.11}$ | 19.15 $^{+0.01}_{-0.02}$ | |
| | b , km/s | 5.9 $^{+0.4}_{-0.6}$ | 0.7 $^{+0.3}_{-0.1}$ | 1.3 $^{+0.1}_{-0.5}$ | 1.4 $^{+0.2}_{-0.3}$ | | |
| H ₂ $J = 1$ | log N | 17.34 $^{+0.42}_{-0.31}$ | 19.24 $^{+0.03}_{-0.01}$ | 17.89 $^{+0.41}_{-0.33}$ | 18.29 $^{+0.09}_{-0.08}$ | 19.31 $^{+0.01}_{-0.01}$ | |
| | b , km/s | † | † | † | † | | |
| H ₂ $J = 2$ | log N | 15.75 $^{+0.15}_{-0.09}$ | 18.45 $^{+0.04}_{-0.04}$ | 16.33 $^{+0.32}_{-0.22}$ | 17.10 $^{+0.18}_{-0.42}$ | 18.47 $^{+0.04}_{-0.04}$ | |
| | b , km/s | 5.9 $^{+1.1}_{-0.3}$ | 1.1 $^{+0.1}_{-0.1}$ | 7.3 $^{+1.0}_{-0.9}$ | 1.5 $^{+0.2}_{-0.1}$ | | |
| H ₂ $J = 3$ | log N | 15.56 $^{+0.10}_{-0.13}$ | 18.23 $^{+0.06}_{-0.10}$ | 15.90 $^{+0.08}_{-0.05}$ | 15.95 $^{+0.38}_{-0.23}$ | 18.24 $^{+0.05}_{-0.10}$ | |
| | b , km/s | 7.7 $^{+0.8}_{-1.1}$ | 1.0 $^{+0.2}_{-0.1}$ | 9.2 $^{+0.9}_{-0.5}$ | 1.6 $^{+0.4}_{-0.2}$ | | |
| H ₂ $J = 4$ | log N | 14.57 $^{+0.09}_{-0.06}$ | 16.32 $^{+0.24}_{-0.21}$ | 14.89 $^{+0.04}_{-0.05}$ | 13.93 $^{+0.25}_{-0.19}$ | 16.34 $^{+0.23}_{-0.19}$ | |
| | b , km/s | 16.8 $^{+2.3}_{-3.3}$ | 1.1 $^{+0.2}_{-0.1}$ | 15.0 $^{+1.1}_{-1.3}$ | 4.3 $^{+3.9}_{-2.4}$ | | |
| H ₂ $J = 5$ | log N | 14.39 $^{+0.09}_{-0.07}$ | 14.35 $^{+0.08}_{-0.06}$ | 14.52 $^{+0.05}_{-0.09}$ | 12.98 $^{+0.44}_{-0.65}$ | 14.91 $^{+0.02}_{-0.02}$ | |
| | b , km/s | 19.1 $^{+4.3}_{-3.3}$ | 4.5 $^{+1.3}_{-0.7}$ | 18.2 $^{+2.2}_{-3.3}$ | 8.0 $^{+7.1}_{-3.1}$ | | |
| | log N_{tot} | 17.87 $^{+0.37}_{-0.33}$ | 19.52 $^{+0.02}_{-0.02}$ | 18.25 $^{+0.22}_{-0.39}$ | 18.57 $^{+0.05}_{-0.09}$ | 19.59 $^{+0.01}_{-0.01}$ | |
| HD $J = 0$ | z | 3.091410($^{+21}_{-14}$) | 3.0915397($^{+66}_{-77}$) | 3.091714($^{+28}_{-48}$) | 3.091871($^{+11}_{-26}$) | | |
| | log N | $\lesssim 12.81$ | 14.82 $^{+0.08}_{-0.08}$ | 14.30 $^{+0.37}_{-0.31}$ | 14.27 $^{+0.10}_{-0.13}$ | 15.02 $^{+0.11}_{-0.07}$ | |
| | b , km/s | 8.0 $^{+4.6}_{-5.4}$ | 5.4 $^{+0.8}_{-0.8}$ | $\lesssim 2.8$ | 4.0 $^{+1.6}_{-1.2}$ | | |
| HD/2H ₂ | | $\lesssim 4.4 \times 10^{-6}$ | $\left(1.0^{+0.3}_{-0.2}\right) \times 10^{-5}$ | $\left(5.6^{+13.7}_{-3.2}\right) \times 10^{-5}$ | $\left(2.5^{+0.9}_{-0.7}\right) \times 10^{-6}$ | $\left(1.34^{+0.39}_{-0.21}\right) \times 10^{-5}$ | |
| log n | | 2.1 $^{+0.5}_{-0.3}$ | 1.7 $^{+0.2}_{-0.2}$ | 1.9 $^{+0.1}_{-0.1}$ | 2.1 $^{+0.2}_{-0.3}$ | | |
| log χ | | 0.9 $^{+0.2}_{-0.2}$ | 1.1 $^{+0.1}_{-0.1}$ | 0.9 $^{+0.1}_{-0.1}$ | 0.6 $^{+0.2}_{-0.2}$ | | |

† The Doppler parameters of H₂ J = 1 was tied to H₂ J = 0.

Table A5. Fit results of H₂ in DLAs at $z = 2.055$ towards J 2340–0053 with seven components.

| comp | | 1 | 2 | 3 | 4 | 5 | 6 | 7 | $\log N_{\text{tot}}$ |
|------------------------|------------|-------------------------------|-------------------------------|-------------------------------|--------------------------------------|--------------------------------------|-------------------------------|--------------------------------------|--------------------------------------|
| z | | 2.0541703($^{+6}_{-4}$) | 2.0542913($^{+4}_{-9}$) | 2.054528($^{+3}_{-3}$) | 2.054610($^{+1}_{-1}$) | 2.054723($^{+3}_{-3}$) | 2.0549952($^{+5}_{-4}$) | 2.0551398($^{+6}_{-4}$) | |
| Δv , km/s | | -54.2 | -42.3 | -19.1 | -11.0 | 0.0 | 26.7 | 40.9 | |
| C I | b , km/s | 2.4 $^{+0.7}_{-0.6}$ | 1.6 $^{+0.6}_{-0.1}$ | 1.9 $^{+0.1}_{-0.1}$ | 1.5 $^{+0.2}_{-0.1}$ | 3.3 $^{+0.2}_{-0.1}$ | 3.9 $^{+1.3}_{-0.9}$ | 3.0 $^{+0.9}_{-0.8}$ | |
| | $\log N$ | 12.27 $^{+0.03}_{-0.05}$ | 12.17 $^{+0.04}_{-0.04}$ | 13.51 $^{+0.04}_{-0.03}$ | 13.20 $^{+0.05}_{-0.04}$ | 13.29 $^{+0.01}_{-0.01}$ | 12.34 $^{+0.05}_{-0.05}$ | 12.42 $^{+0.05}_{-0.02}$ | 13.89 $^{+0.01}_{-0.02}$ |
| | C I* | 11.97 $^{+0.08}_{-0.13}$ | 12.29 $^{+0.05}_{-0.05}$ | 13.06 $^{+0.01}_{-0.01}$ | 12.67 $^{+0.02}_{-0.03}$ | 12.97 $^{+0.01}_{-0.01}$ | 11.72 $^{+0.15}_{-0.22}$ | 12.18 $^{+0.06}_{-0.07}$ | 13.48 $^{+0.01}_{-0.01}$ |
| | C I** | < 10.7 | 12.06 $^{+0.07}_{-0.09}$ | < 11.0 | < 11.0 | 12.19 $^{+0.06}_{-0.05}$ | < 11.0 | < 10.6 | 12.47 $^{+0.05}_{-0.04}$ |
| $\log N_{\text{tot}}$ | | 12.46 $^{+0.02}_{-0.06}$ | 12.66 $^{+0.03}_{-0.03}$ | 13.66 $^{+0.02}_{-0.03}$ | 13.32 $^{+0.04}_{-0.04}$ | 13.48 $^{+0.01}_{-0.01}$ | 12.43 $^{+0.06}_{-0.06}$ | 12.61 $^{+0.04}_{-0.03}$ | 14.04 $^{+0.01}_{-0.01}$ |
| cft† | | | | 0.86 $^{+0.02}_{-0.02}$ | 0.94 $^{+0.04}_{-0.02}$ | 0.92 $^{+0.03}_{-0.02}$ | | | |
| H ₂ $J = 0$ | $\log N$ | 15.30 $^{+0.03}_{-0.07}$ | 14.22 $^{+0.09}_{-0.05}$ | 16.45 $^{+0.19}_{-0.14}$ | 17.58 $^{+0.09}_{-0.08}$ | 17.50 $^{+0.05}_{-0.07}$ | 15.59 $^{+0.04}_{-0.05}$ | 16.78 $^{+0.05}_{-0.07}$ | 17.90 $^{+0.03}_{-0.03}$ |
| | b , km/s | 2.5 $^{+0.1}_{-0.1}$ | 1.7 $^{+0.1}_{-0.2}$ | 3.0 $^{+0.1}_{-0.2}$ | 1.0 $^{+0.1}_{-0.3}$ | 3.1 $^{+0.1}_{-0.1}$ | 3.8 $^{+0.1}_{-0.1}$ | 1.8 $^{+0.1}_{-0.1}$ | |
| H ₂ $J = 1$ | $\log N$ | 15.85 $^{+0.05}_{-0.04}$ | 14.99 $^{+0.06}_{-0.04}$ | 16.90 $^{+0.18}_{-0.09}$ | 18.13 $^{+0.06}_{-0.06}$ | 18.03 $^{+0.04}_{-0.04}$ | 16.28 $^{+0.04}_{-0.03}$ | 17.31 $^{+0.03}_{-0.05}$ | 18.43 $^{+0.02}_{-0.02}$ |
| | b , km/s | ‡ | ‡ | ‡ | ‡ | ‡ | ‡ | ‡ | |
| H ₂ $J = 2$ | $\log N$ | 14.67 $^{+0.06}_{-0.03}$ | 14.36 $^{+0.02}_{-0.03}$ | 15.74 $^{+0.06}_{-0.07}$ | 17.15 $^{+0.14}_{-0.21}$ | 16.20 $^{+0.04}_{-0.06}$ | 15.45 $^{+0.03}_{-0.03}$ | 15.72 $^{+0.06}_{-0.06}$ | 17.20 $^{+0.14}_{-0.14}$ |
| | b , km/s | 2.4 $^{+0.2}_{-0.1}$ | 4.8 $^{+0.6}_{-0.4}$ | 3.6 $^{+0.2}_{-0.1}$ | 1.9 $^{+0.2}_{-0.3}$ | 4.8 $^{+0.1}_{-0.1}$ | 4.4 $^{+0.2}_{-0.1}$ | 2.3 $^{+0.1}_{-0.1}$ | |
| H ₂ $J = 3$ | $\log N$ | 14.15 $^{+0.03}_{-0.04}$ | 14.38 $^{+0.02}_{-0.02}$ | 15.03 $^{+0.04}_{-0.06}$ | 15.28 $^{+0.04}_{-0.08}$ | 15.76 $^{+0.02}_{-0.02}$ | 15.14 $^{+0.01}_{-0.03}$ | 14.61 $^{+0.04}_{-0.02}$ | 16.03 $^{+0.02}_{-0.01}$ |
| | b , km/s | 2.8 $^{+0.3}_{-0.3}$ | 5.6 $^{+0.5}_{-0.5}$ | 4.6 $^{+0.3}_{-0.3}$ | 5.5 $^{+1.2}_{-0.9}$ | 5.4 $^{+0.1}_{-0.1}$ | 4.7 $^{+0.1}_{-0.2}$ | 2.8 $^{+0.2}_{-0.2}$ | |
| H ₂ $J = 4$ | $\log N$ | 12.62 $^{+0.65}_{-0.46}$ | 13.68 $^{+0.06}_{-0.13}$ | 13.88 $^{+0.06}_{-0.08}$ | 13.41 $^{+0.17}_{-0.34}$ | 14.43 $^{+0.02}_{-0.03}$ | 14.00 $^{+0.04}_{-0.06}$ | 13.33 $^{+0.18}_{-0.19}$ | 14.73 $^{+0.01}_{-0.02}$ |
| | b , km/s | 6.2 $^{+4.0}_{-2.2}$ | 12.0 $^{+2.7}_{-5.3}$ | 6.4 $^{+1.2}_{-1.1}$ | 5.8 $^{+2.3}_{-1.1}$ | 7.7 $^{+0.5}_{-0.5}$ | 7.6 $^{+1.6}_{-0.9}$ | 7.3 $^{+2.2}_{-3.4}$ | |
| H ₂ $J = 5$ | $\log N$ | 12.35 $^{+0.94}_{-0.58}$ | 13.93 $^{+0.12}_{-0.12}$ | 13.60 $^{+0.17}_{-0.13}$ | 12.31 $^{+0.43}_{-0.83}$ | 14.15 $^{+0.05}_{-0.03}$ | 13.66 $^{+0.12}_{-0.15}$ | 13.07 $^{+0.31}_{-0.35}$ | 14.54 $^{+0.02}_{-0.04}$ |
| | b , km/s | 12.9 $^{+3.4}_{-5.2}$ | 17.6 $^{+1.8}_{-4.2}$ | 7.9 $^{+5.9}_{-1.9}$ | 10.0 $^{+2.1}_{-3.8}$ | 7.5 $^{+0.8}_{-0.5}$ | 15.8 $^{+3.2}_{-3.3}$ | 10.4 $^{+1.3}_{-5.2}$ | |
| $\log N_{\text{tot}}$ | | 15.99 $^{+0.04}_{-0.04}$ | 15.24 $^{+0.04}_{-0.03}$ | 17.11 $^{+0.12}_{-0.14}$ | 18.27 $^{+0.06}_{-0.06}$ | 18.14 $^{+0.04}_{-0.04}$ | 16.43 $^{+0.03}_{-0.03}$ | 17.43 $^{+0.04}_{-0.05}$ | 18.57 $^{+0.02}_{-0.02}$ |
| HD $J = 0$ | $\log N$ | $\lesssim 13.51$ | $\lesssim 12.69$ | $\lesssim 13.76$ | 13.60 $^{+0.15}_{-0.14}$ | 13.84 $^{+0.05}_{-0.05}$ | $\lesssim 12.58$ | 13.29 $^{+0.15}_{-0.21}$ | 14.11 $^{+0.06}_{-0.06}$ |
| | b , km/s | 2.5 $^{+0.1}_{-0.1}$ | 1.7 $^{+0.1}_{-0.2}$ | 3.0 $^{+0.1}_{-0.2}$ | 1.0 $^{+0.1}_{-0.3}$ | 3.1 $^{+0.1}_{-0.1}$ | 3.8 $^{+0.1}_{-0.1}$ | 1.8 $^{+0.1}_{-0.1}$ | |
| HD/2H ₂ | | $\lesssim 1.7 \times 10^{-3}$ | $\lesssim 1.4 \times 10^{-3}$ | $\lesssim 2.2 \times 10^{-4}$ | $(1.1^{+0.5}_{-0.3}) \times 10^{-5}$ | $(2.5^{+0.4}_{-0.3}) \times 10^{-5}$ | $\lesssim 7.1 \times 10^{-5}$ | $(3.6^{+1.6}_{-0.3}) \times 10^{-5}$ | $(1.7^{+0.3}_{-0.2}) \times 10^{-5}$ |
| $\log n$ | | | | 0.8 $^{+0.3}_{-0.3}$ | 0.6 $^{+0.3}_{-0.4}$ | 1.2 $^{+0.1}_{-0.1}$ | | 0.8 $^{+0.3}_{-0.5}$ | |
| $\log \chi$ | | | | 0.1 $^{+0.2}_{-0.2}$ | -0.2 $^{+0.2}_{-0.2}$ | 0.5 $^{+0.1}_{-0.1}$ | | -0.2 $^{+0.2}_{-0.2}$ | |

† covering factors used for C I ~ 1560 Å lines.

‡ The Doppler parameters of H₂ $J = 1$ was tied to H₂ $J = 0$.

**APPENDIX B: 1D AND 2D POSTERIORS ON
PHYSICAL CONDITIONS**

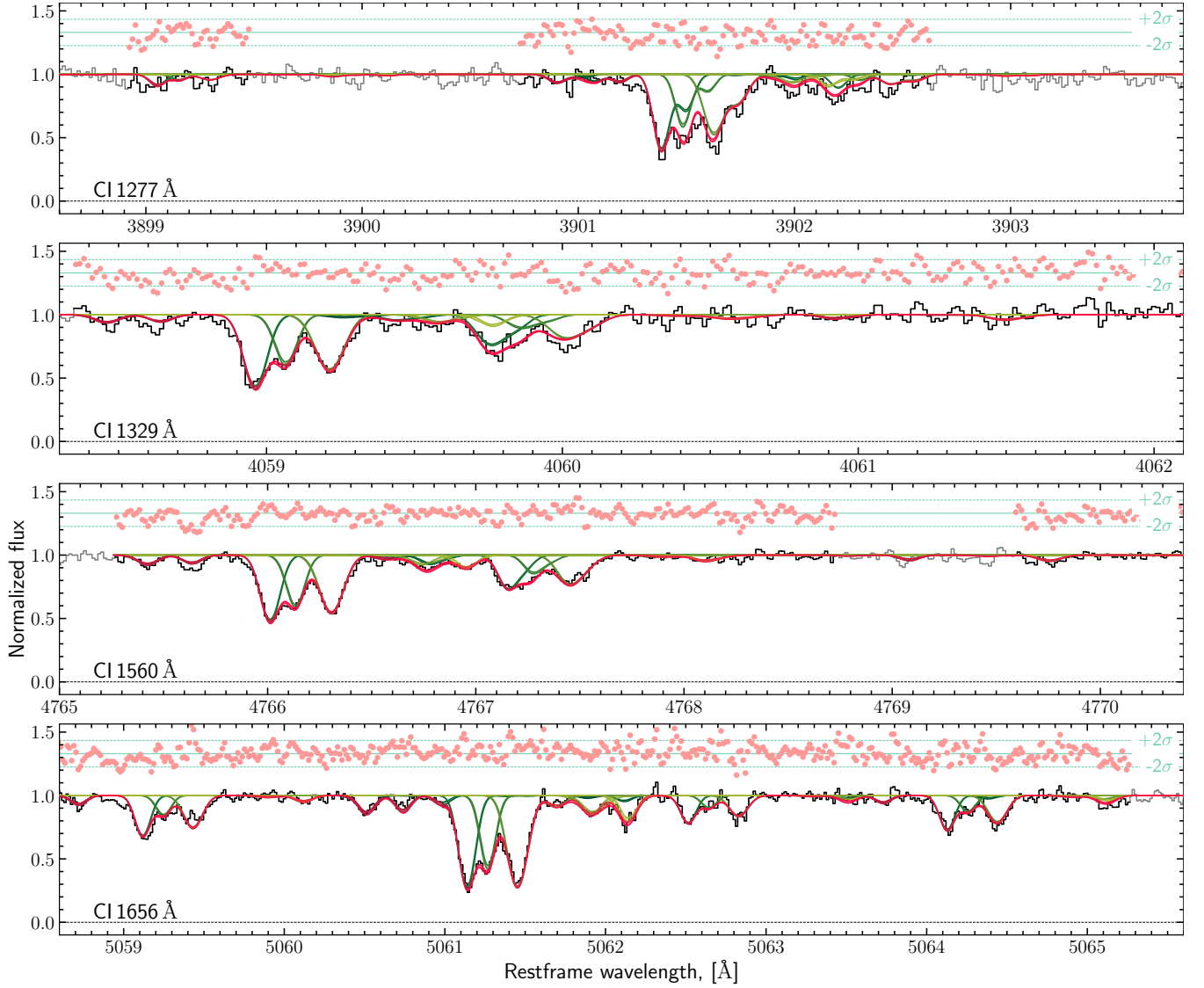


Figure A25. Fit to C I absorption lines in DLA at 2.05 towards J 2340–0053. The lines are the same as in Fig. A1.

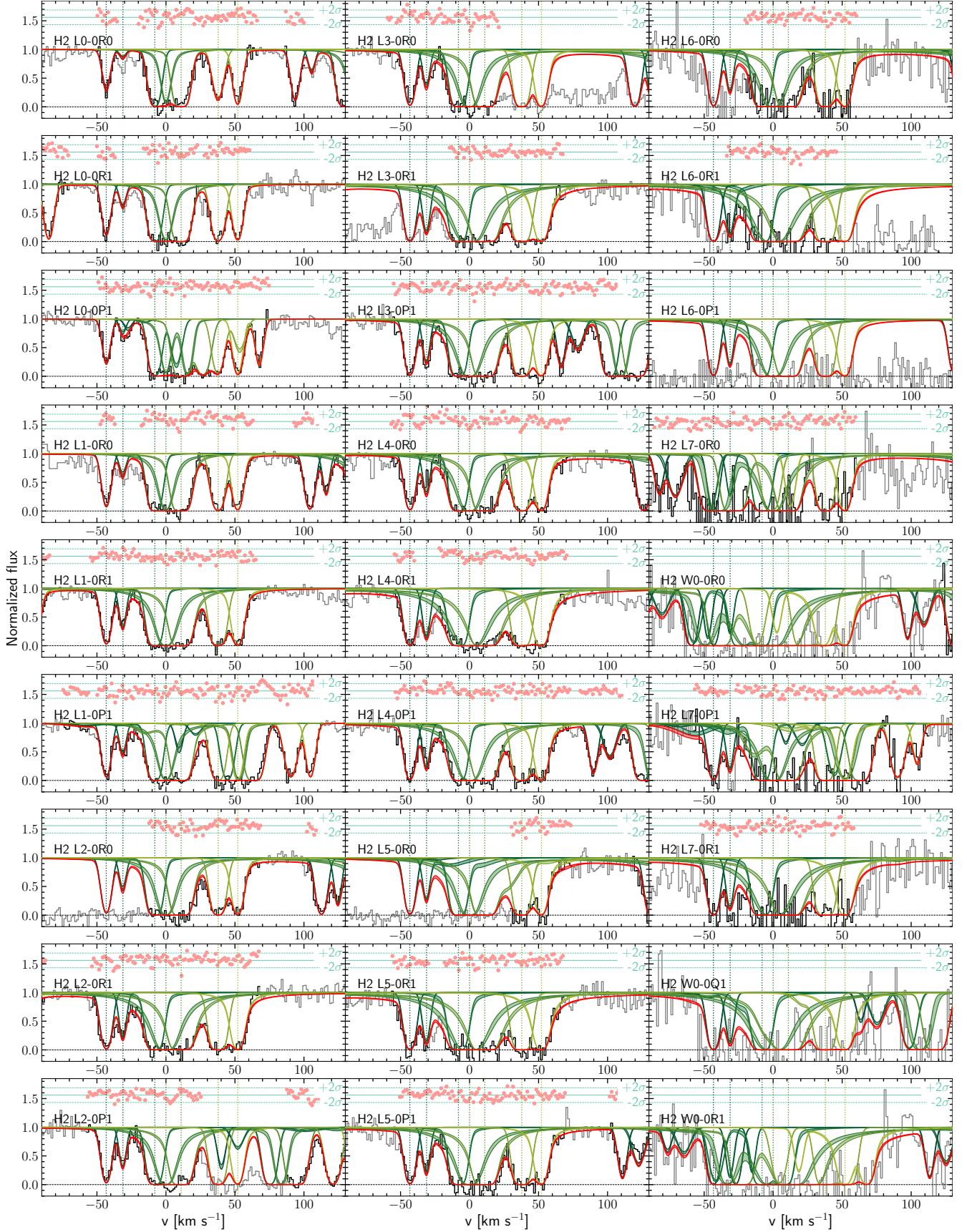


Figure A26. Fit to H₂ absorption lines of transitions from $J = 0$ and $J = 1$ rotational levels in DLA at 2.05 towards J 2340–0053. The lines are the same as in Fig. A1.

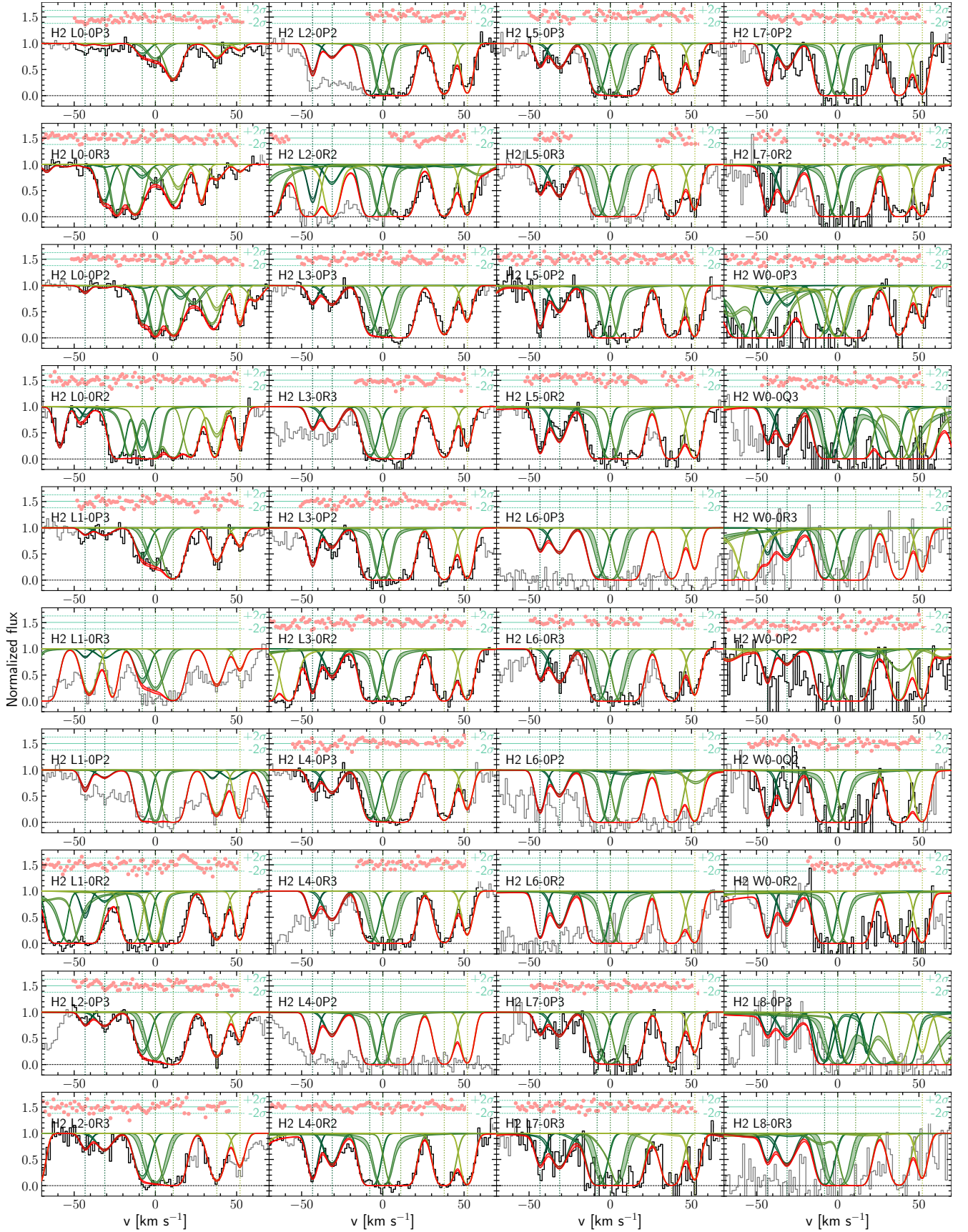


Figure A27. Fit to H₂ absorption lines of transitions from $J = 2$ and $J = 3$ rotational levels in DLA at 2.05 towards J 2340–0053. The lines are the same as in Fig. A1.

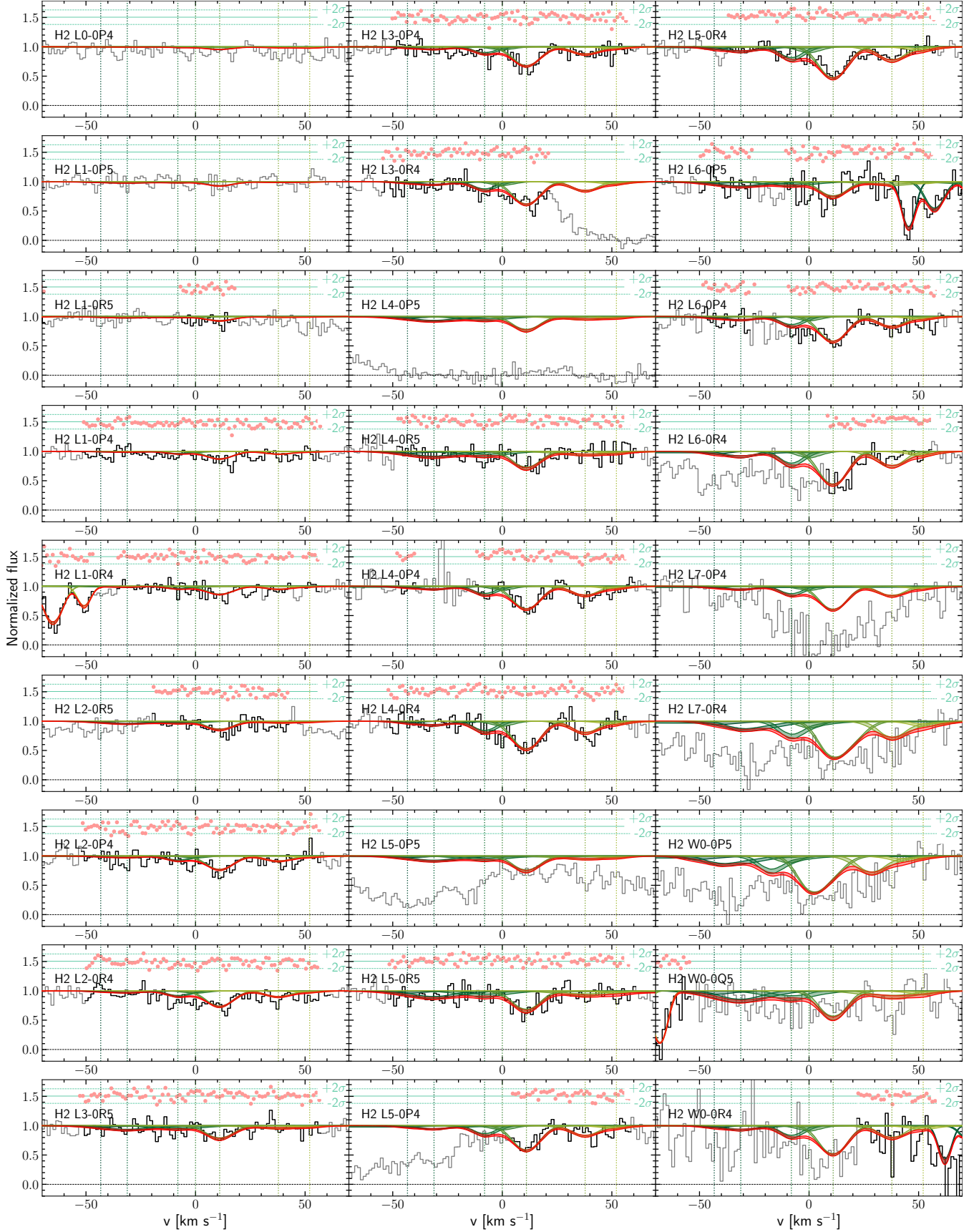


Figure A28. Fit to H₂ absorption lines of transitions from $J = 4$ and $J = 5$ rotational levels in DLA at 2.05 towards J 2340–0053. The lines are the same as in Fig. A1.

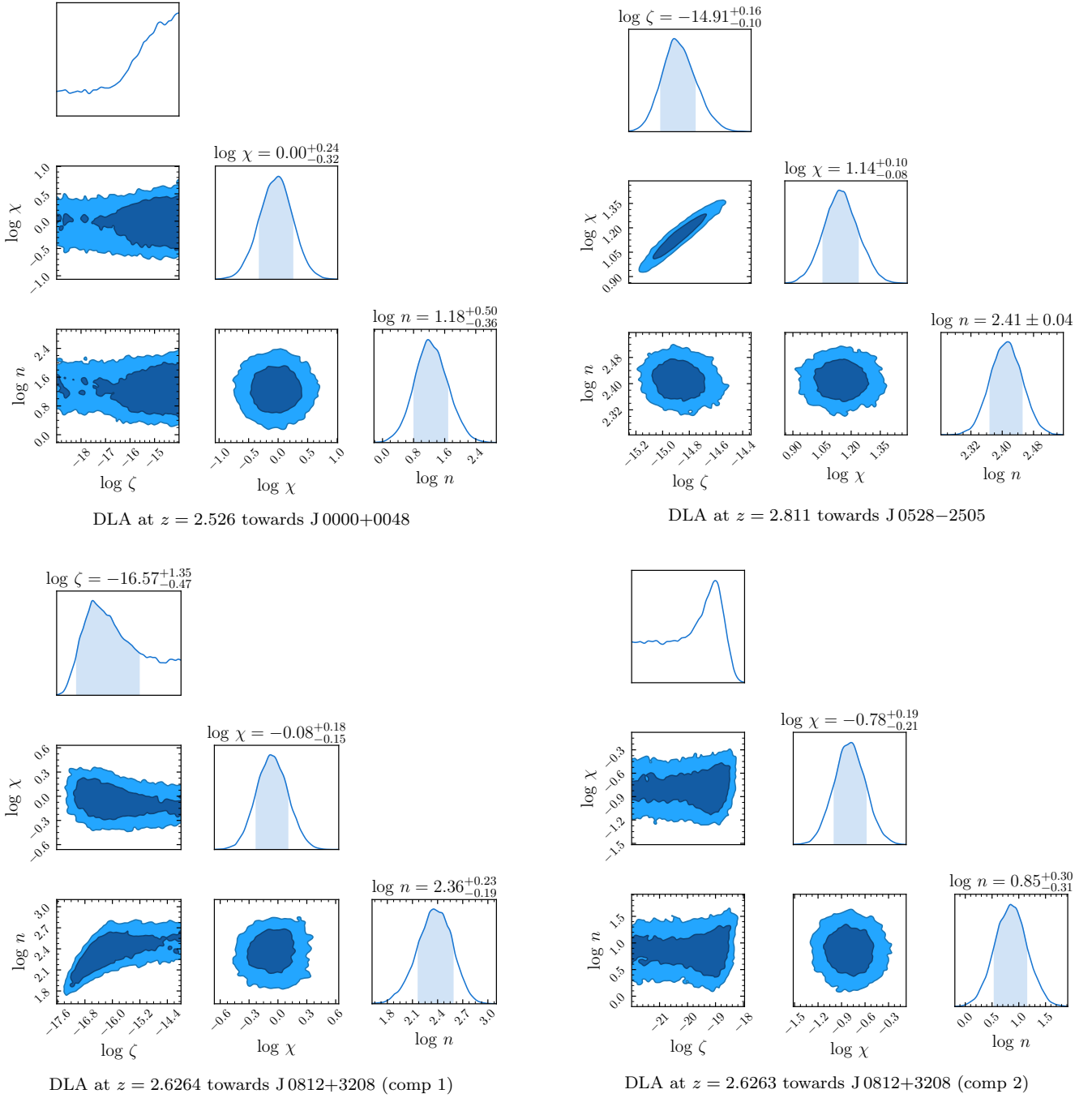


Figure B1. The marginalized posterior probability functions for CRIR, UV field strength, and number density, obtained from fitting measured $N_{\text{HD}}/N_{\text{H}_2}$ in the systems at high redshift. The diagonal panels on each subplot indicate 1d posterior function, where the blue shade area corresponds to 0.68 confidence level. The non-diagonal panels show the 2d posterior function, where dark and light blue regions correspond to 0.68 and 0.95 confidence levels.

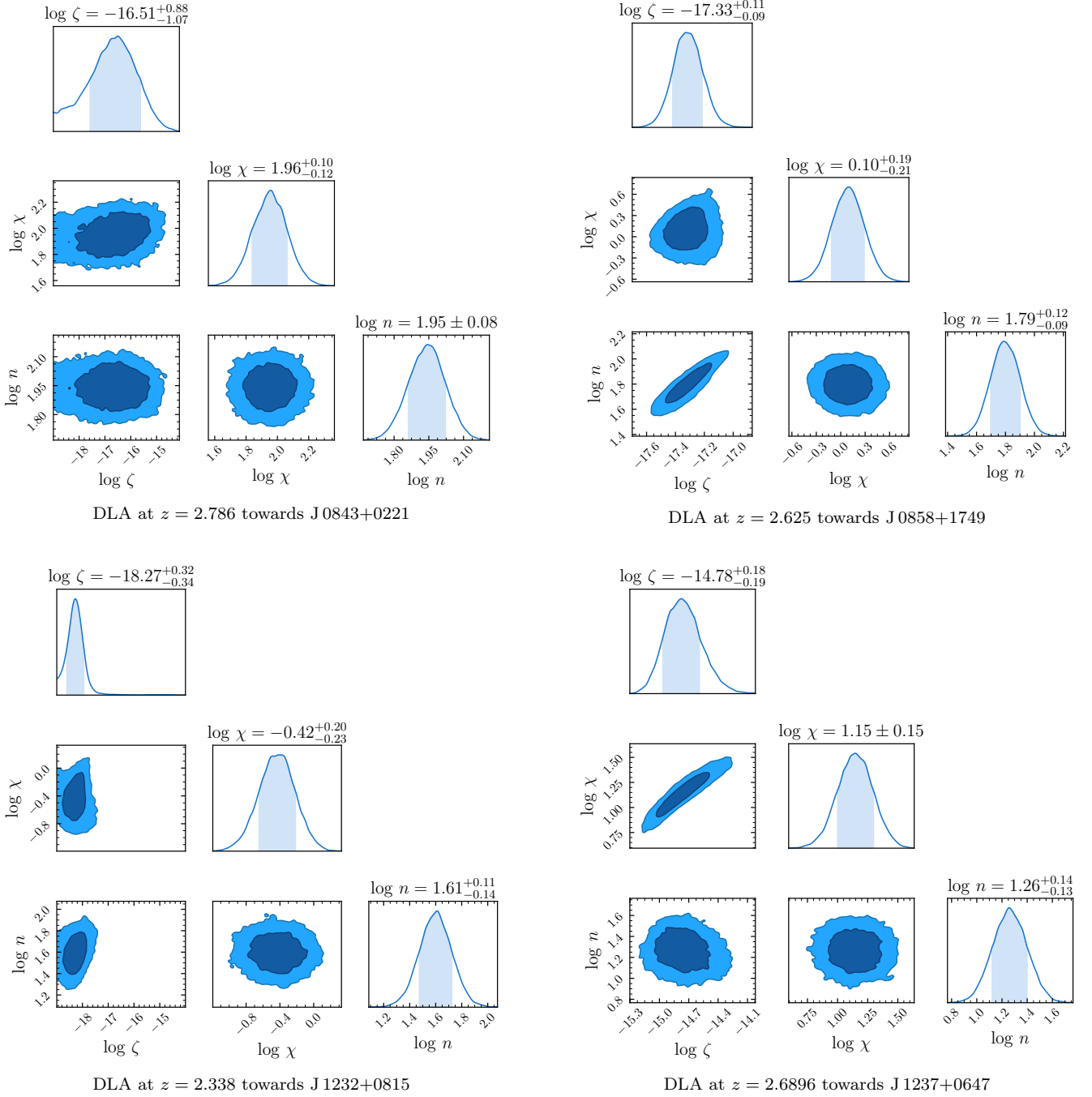


Figure B2. The marginalized posterior probability functions for CRIR, UV field strength, and number density (continued).

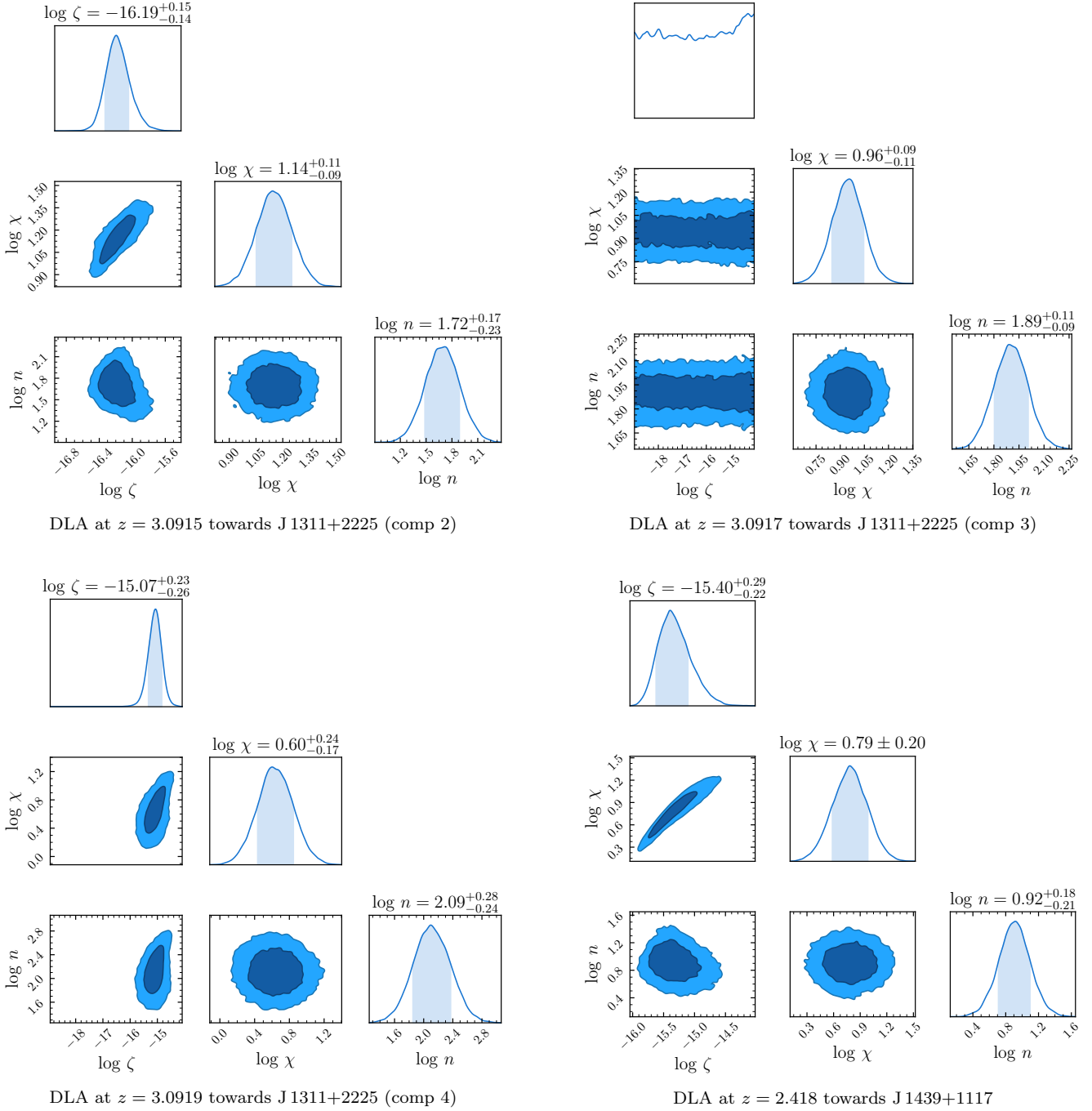


Figure B3. The marginalized posterior probability functions for CRIR, UV field strength, and number density (continued).

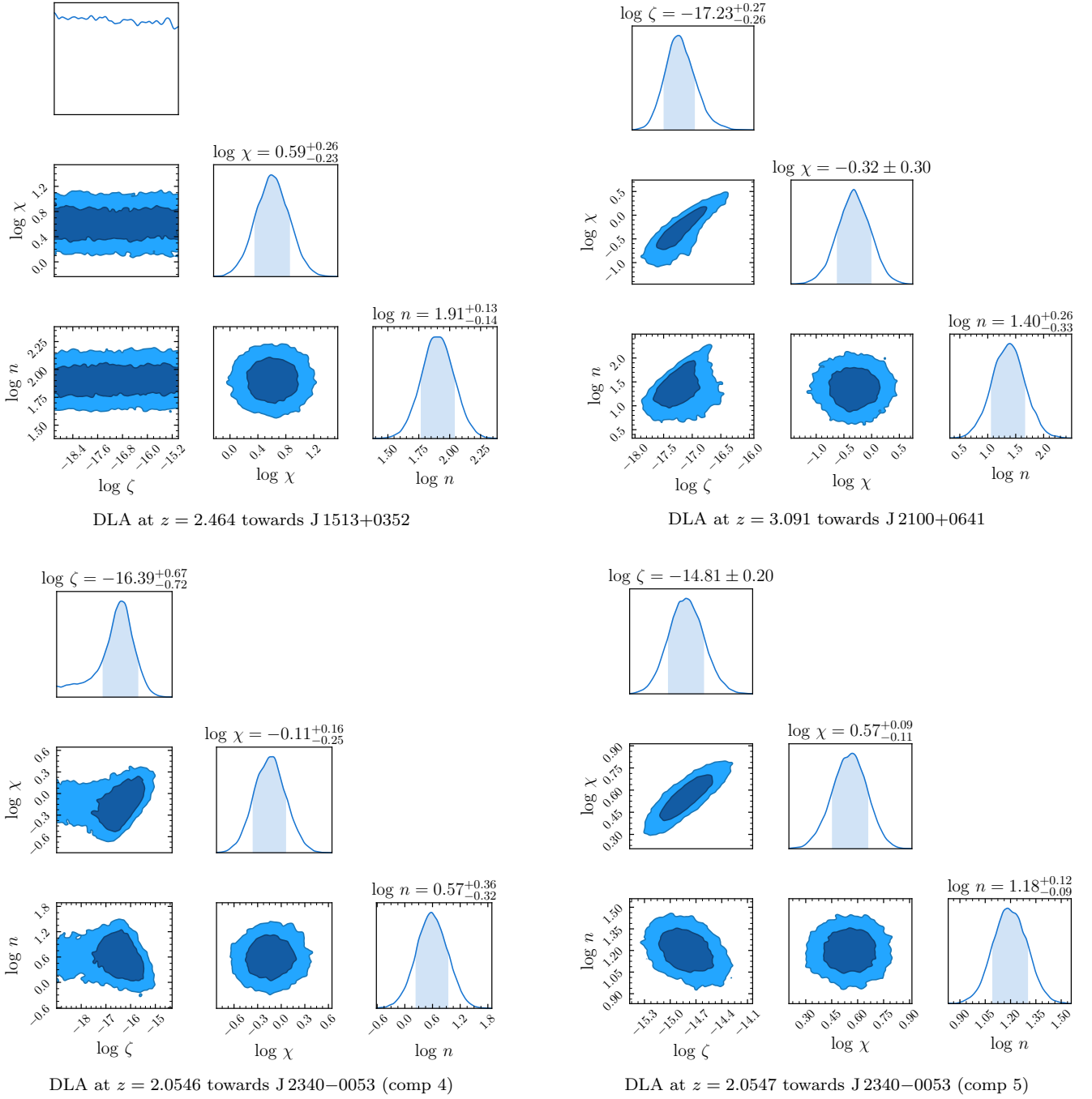


Figure B4. The marginalized posterior probability functions for CRIR, UV field strength, and number density (continued).

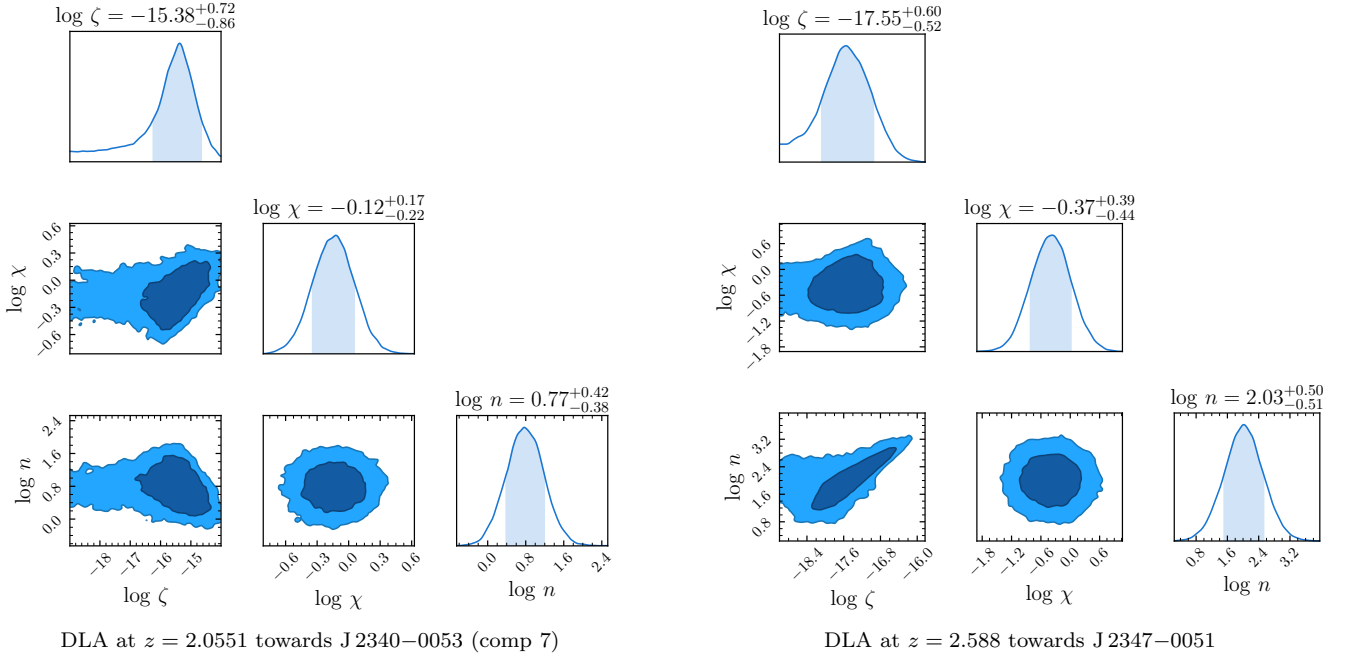


Figure B5. The marginalized posterior probability functions for CRIR, UV field strength, and number density (continued).